

Electronic Supplementary Information

Repurposing a peptide antibiotic as a catalyst: multicopper–daptomycin complex as a cooperative O–O bond formation and activation catalyst

Yen Jea Lee,^{a,†} Haesol Kim,^{b,†} Yujeong Kim,^{c, d, †} Kang Hee Cho,^{e, †} Sugyeong Hong,^{c, d} Ki Tae Nam,^{e, *} Sun Hee Kim,^{c, d, *} Chang Hyuck Choi,^{f, *} and Jiwon Seo^{a, *}

^a Department of Chemistry, ^b School of Materials Science and Engineering, Gwangju Institute of Science and Technology, Gwangju 61005, Republic of Korea

^c Western Seoul Center, Korea Basic Science Institute, Seoul 03759, Republic of Korea

^d Department of Chemistry and Nano Science, Ewha Womans University, Seoul 03760, Republic of Korea

^e Department of Materials Science and Engineering, Seoul National University, Seoul 08826, Republic of Korea

^f Department of Chemistry, Pohang University of Science and Technology, Pohang 37673, Republic of Korea

†These authors contributed equally to this work.

*Corresponding author:

Jiwon Seo, Ph.D. (email: jseo@gist.ac.kr)

Chang Hyuck Choi, Ph.D. (email: chchoi@postech.ac.kr)

Sun Hee Kim, Ph.D. (email: shkim7@kbsi.re.kr)

Ki Tae Nam, Ph.D. (email: nkitae@snu.ac.kr)

Table of Contents

1. Materials	S3
2. General methods	S4
3. Preparation of the Cu _n -daptomycin complex	S6
4. Job plot	S7
5. Cu(II) binding constant of Cu _n -dap complexes	S8
6. Kinetic study of daptomycin linearization	S10
7. ESI-HRMS analysis of Cu _n -dap complexes	S13
8. Electron paramagnetic resonance (EPR) spectroscopy	S17
9. Evans method	S23
10. Synthesis of the tetra-methyl ester derivative of daptomycin	S24
11. Comparison between daptomycin and the tetra-methyl ester derivative 5 in metallation	S27
12. Cu(0/I/II) redox state assignment of Cu _n -dap complexes	S28
13. Ascorbic acid oxidation	S33
14. 2,6-Dimethoxyphenol oxidation	S36
15. O ₂ evolution measurement during H ₂ O ₂ disproportionation with Cu _n -dap.	S38
16. Hydroxyl radical detection using 2,7-dichlorofluorescein diacetate	S40
17. Electrochemical analysis	S43
18. Differential pulse voltammetry (DPV)	S45
19. The scan rate dependence of observed currents with Cu ₄ -dap in CV	S46
20. Faradaic efficiency evaluation during water electrolysis	S47
21. <i>In situ</i> UV-vis spectroscopy	S50
22. <i>In situ</i> Raman spectroscopy	S51
23. Kinetic isotope effect in CV measurement	S54
24. A plausible reaction pathway for O–O bond formation mediated by Cu ₄ -dap	S54
25. References	S55

1. Materials

The solvents and reagents were purchased from commercial vendors and used without further purification. Daptomycin, tetraglycine, trisodium nitrilotriacetate monohydrate, H₂O₂ (35% wt in H₂O) and NaOH were purchased from TCI, Tokyo, Japan. CuCl₂, NiCl₂·6H₂O, CoCl₂·6H₂O, FeCl₂, Fe(NO₃)₃·9H₂O, MnCl₂·4H₂O, HCl (37% wt in H₂O), sodium phosphate dibasic, triglycine, ascorbic acid (Acs), 2,6-dimethoxyphenol (DMP), di-*tert*-butyl dicarbonate (Boc₂O), anhydrous MeOH, anhydrous CH₂Cl₂, 4-(dimethylamino)pyridine (DMAP), 2',7'-dichlorofluorescein diacetate (DCFH-DA), and H₂¹⁸O were purchased from Sigma Aldrich, MO, USA. D₂O was purchased from Cambridge Isotope Laboratories, Inc., MA, USA. Pivalic anhydride was purchased from Alfa Aesar, MA, USA. CH₃CN (HPLC grade), *N,N*-dimethylformamide (DMF) and trifluoroacetic acid (TFA) were purchased from Thermo Fisher Scientific, NH, USA. Ultrapure water (> 18.2 MΩ, aqua MAXTM-Ultra 370 series, YOUNGLIN) was used to prepare the HPLC eluent or metal-peptide complex for spectroscopy and electrochemical analysis.

2. General methods

2.1. Absorption/fluorescence spectroscopy

The UV-vis spectra were obtained by using an Ultrospec 2100 pro UV-vis spectrophotometer (GE Healthcare, Buckinghamshire, UK) with a 1 cm path-length quartz cuvette at room temperature. For the kinetic study, Infinite 200Pro (Tecan, Männedorf, CH) equipped with Tecan *i*-control was used for the absorbance with a quartz or polypropylene 96-well plate. A Synergy H1 microplate plate reader (BioTek Instruments Inc., VT, USA) with a 96-well microplate was used to record fluorescence spectra.

2.2. High-performance liquid chromatography (HPLC)

For the HPLC analysis, a Waters HPLC system (Waters Corporation, MA, USA) equipped with a reversed-phase (RP) column (SunFire C18, 4.6 × 250 mm, 5 μm), Waters 2489 UV/Visible detector, Waters 1525 Binary HPLC Pump, Waters 2707 Autosampler, and Waters 5CH column oven was used. The detector was set to monitor sample elution at 220 nm. The mobile phases were H₂O (A, +0.1% TFA) and CH₃CN (B, +0.1% TFA). The column oven temperature was 40 °C. A Waters preparative HPLC system (Waters PrepLC system, Waters 2489 UV/Visible detector, and Waters fraction collector III) was used to purify a peptide with a C₁₈ preparative HPLC column (SunFire C18, 19 x 150 mm, 5 μm). HPLC gradient methods; **method 1**: eluent gradient was held at 5% B for 2 min and ramped to 100% over 30 min with a flow rate of 1 mL/min; **method 2**: eluent gradient was held at 5% B for 5 min and ramped to 100% over 20 min with a flow rate of 14 mL/min.

2.3. Ultra-performance liquid chromatography (UPLC)

A Waters Acquity UPLC system (Waters Corp., MA, USA) was used to analyze peptoid oligomers. The Waters UPLC system was equipped with a reverse-phase column (Acquity UPLC® BEH C₁₈ 1.7 μm, 2.1 × 50 mm), Acquity-TUV Detector, Acquity-Solvent Manager

FTN-H, and Acquity-Quaternary Solvent Manager. The mobile phases were water (A, 0.1% TFA, v/v) and acetonitrile (ACN) (B, 0.1% TFA, v/v). The flow rate was 0.6 mL/min. The chromatograms were recorded with a detection wavelength at 220 nm. The following conditions were used for peptoid sample analysis. The column was preheated at 40 °C. Before the sample injection, the column was conditioned with 5% of B. After the sample injection (2 μ L), 5% B was kept for 1 min, and the linear gradient of 5–60% of B was applied for 7 min.

2.4. Liquid chromatography-mass spectrometry (LC-MS)

The mass data of the peptides were obtained using an Agilent LC-MS system (Agilent Technologies, Inc., CA, USA) equipped with a 1260 Infinity LC and 6120 SQ bundle system with an API-electrospray ion source.

3. Preparation of the Cu_n-daptomycin complex

Daptomycin (dap, 1 μmol) was dissolved in Na₂HPO₄ buffer (0.1M, pH 11.5, 0.9 mL). To the daptomycin solution were added corresponding equivalent of CuCl₂ (1.0 M stock solution in H₂O). Then pH was adjusted to pH 11.5 using NaOH (1.0 M, aq) to compensate the pH drop due to CuCl₂ addition. The resulting solution volume was made up to 1 mL with the buffer to afford Cu_n-dap solution (1 mM). The prepared solution was mixed on a 2-D orbital shaker with 140 rpm shaking overnight. Then, using centrifugation at 10,000 rpm for 5 min, Cu precipitate, expected as Cu(OH)₂ or Cu₃(PO₄)₂, removed, since when over 4 equiv CuCl₂ was added, there is apparent blue precipitates as shown in Figure S1. Linear daptomycin was obtained by incubating daptomycin (1 mM) in Na₂HPO₄ buffer (0.1 M, pH 11.5) at 4 °C for 12 h (Figure S2).

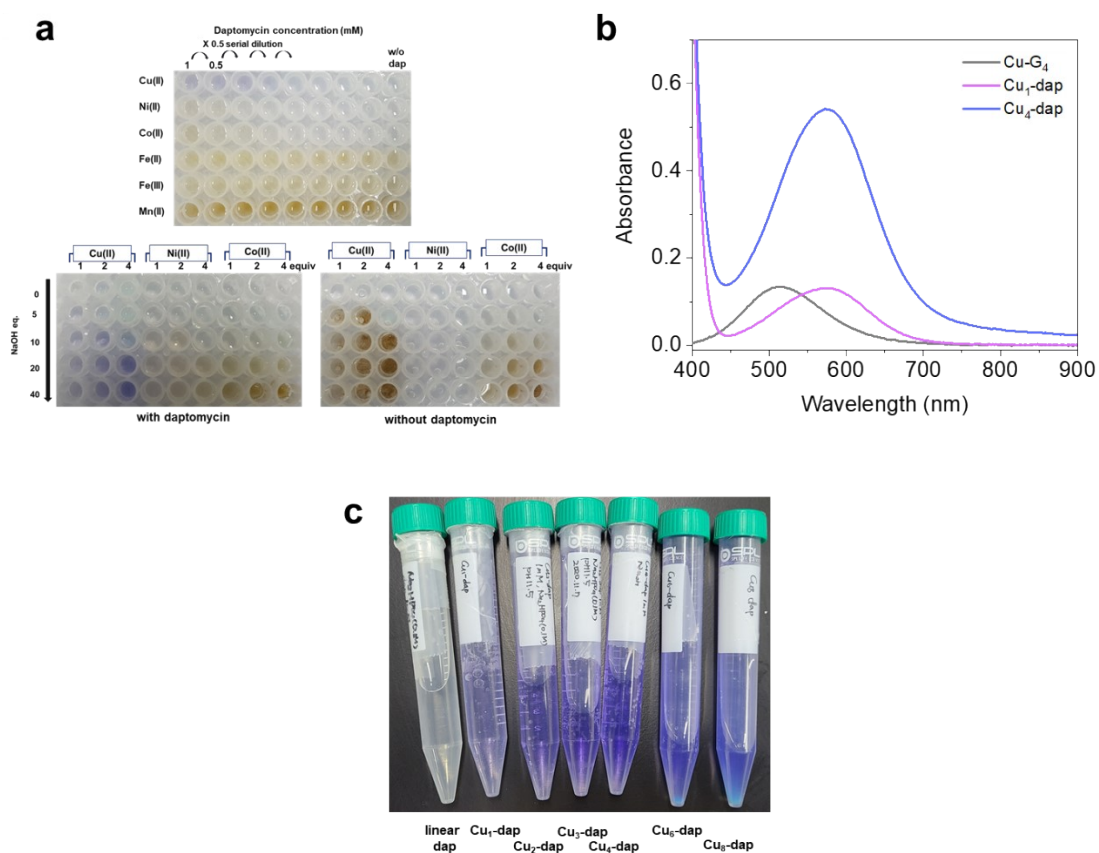


Figure S1. (a) Screening of metal-binding between daptomycin and redox-active metals

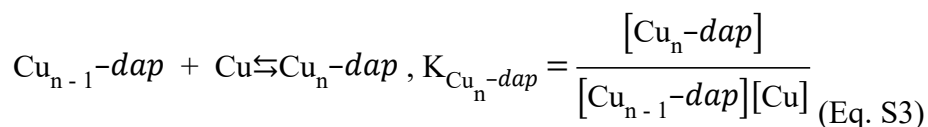
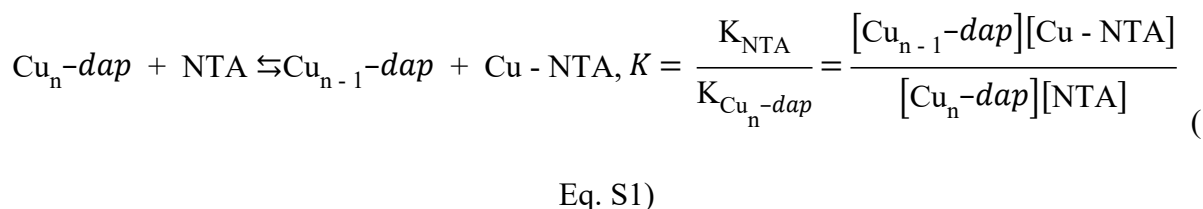
(Cu(II), Ni(II), Co(II), Fe(II), Fe(III), and Mn(II)). (top) The complexation was tested in Na_2HPO_4 buffer (0.1 M, pH 11.5), in the presence of metal salt (1 mM, used metal salts: CuCl_2 , $\text{NiCl}_2 \cdot 6\text{H}_2\text{O}$, $\text{CoCl}_2 \cdot 6\text{H}_2\text{O}$, FeCl_2 , $\text{Fe}(\text{NO}_3)_3 \cdot 9\text{H}_2\text{O}$, and $\text{MnCl}_2 \cdot 4\text{H}_2\text{O}$) and daptomycin. The highest concentration of daptomycin was 1 mM, and it was serially diluted with a factor of 0.5). (bottom) Screening of the complexation between daptomycin (1 mM) and three different metal salts (Cu(II), Ni(II), and Co(II); 1, 2, and 4 equivalents were added.) under the addition of five different equivalents of NaOH (0, 5, 10, 20, and 40 equiv) in water. Distinct color change upon Cu(II)–daptomycin complexation was observed. (b) UV-vis spectra of Cu-peptide complexes (1 mM) in sodium phosphate buffer (0.1 M, pH 11.5, $I = 0.44$ M). (c) Photographs of Cu_n –dap solutions (1 mM) in Na_2HPO_4 buffer (0.1 M, pH 11.5, $I = 0.44$ M).

4. Job plot

Job plot, or continuous variation method was used to investigate the binding stoichiometry of the complexation between Cu(II) and daptomycin. The total concentration of $[\text{CuCl}_2]$ and $[\text{daptomycin}]$ was fixed to 1 mM in Na_2HPO_4 buffer (0.1 M, 500 μL , pH 11.5, $I = 0.44$ M) at 25 °C. The molar fraction of Cu(II) was varied from 0 to 1. The absorbance at 576 nm was measured using a UV-vis spectrophotometer with an 1 cm path-length cuvette and plotted along with a molar fraction of Cu(II). The maximum of the absorbance was observed at a molar fraction of Cu(II) of 0.79 in Figure 2b, which indicated that the preferred binding mode is 4:1 (Cu(II):daptomycin).

5. Cu(II) binding constant of Cu_n-dap complexes

A competitive ligand for Cu(II), nitrilotriacetic acid (NTA), was used to evaluate a binding constant for the outermost Cu site of each Cu_n-dap (n = 1–4). The apparent binding affinity of NTA for Cu(II) was calculated using the IUPAC stability constant database (Mini-SCDatabase) built in SolEq software (Academic software, Otley, UK).¹ Ionic strength (based on the Davis equation) and temperature dependence (based on the Van't Hoff equation) for the binding constants were calculated using SolEq software. At pH 11.5, the calculated pK_{app} of NTA for Cu(II) is 14.6 at 25 °C (*I* = 0.44 M). The spectrophotometric titration data was obtained by measuring the characteristic absorbance of Cu-NTA at 800 nm using a TECAN microplate reader. NTA stock solution (20 mM) was titrated into Cu_n-dap solution (1 mM, 200 μL) in Na₂HPO₄ buffer. All measurements were triplicated for each complex. From the standard curve plotting the measured absorbance versus Cu-NTA (μmol) (Fig. S3(a)), we calculated the existing Cu-NTA during titration. Based on Eq. S1–5, the Cu binding constant of the outermost Cu(II) site was calculated as shown in Table S1.



$$K = \frac{K_{\text{NTA}}}{K_{\text{Cu}_n\text{-dap}}}, K_{\text{Cu}_n\text{-dap}} = \frac{1}{K} K_{\text{NTA}}, \quad (\text{Eq. S4})$$

$$\text{when } [\text{Cu} - \text{NTA}] = [\text{Cu}_n\text{-dap}], K = \frac{K_{\text{NTA}}}{K_{\text{Cu}_n\text{-dap}}} = \frac{[\text{Cu} - \text{NTA}]}{[\text{NTA}]} = \frac{[\text{Cu} - \text{NTA}]}{[\text{NTA}]_0 - [\text{Cu} - \text{NTA}]} \quad (\text{Eq. S5})$$

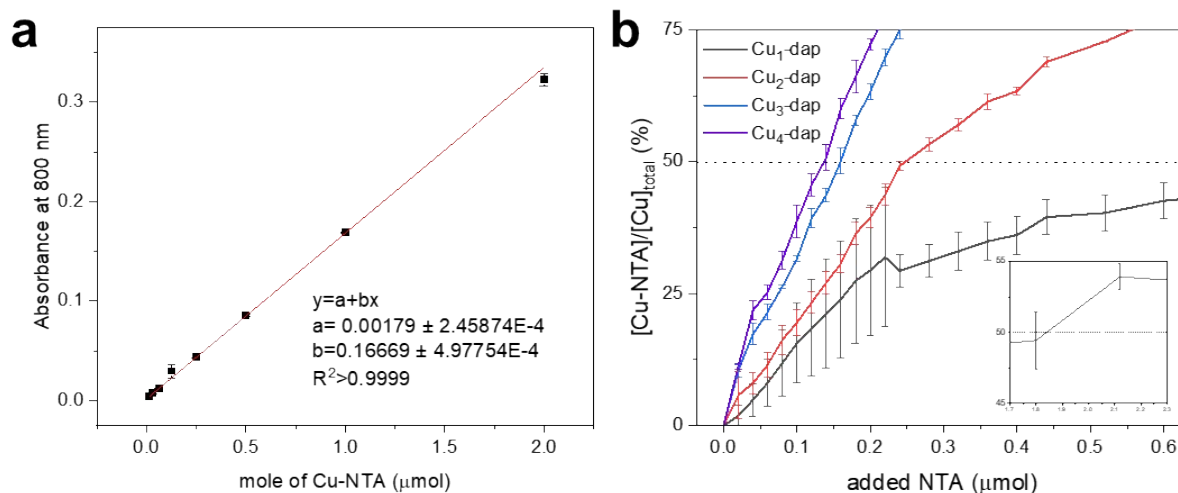


Figure S2. (a) The obtained standard curve plotting absorbance at 800 nm versus Cu-NTA (μmol). (b) The formation of Cu-NTA complex (%) versus added NTA to calculate the binding constant during titrations. The error bars were calculated from the triplicated experiments.

Table S1. The calculated relative Cu(II) binding constants.^a

	Cu ₁ -dap	Cu ₂ -dap	Cu ₃ -dap	Cu ₄ -dap
$\log^{[10]}(K_{\text{Cu}_n\text{-dap}})$	15.7 ± 0.16	14.8 ± 0.03	14.4 ± 0.04	13.8 ± 0.28

^a Standard deviation values were calculated from triplicated experiments.

6. Kinetic study of daptomycin linearization

Daptomycin (1 mM, 200 μ L) with or without 4 equivalents of Cu(II) ions was incubated in Na_2HPO_4 buffer (0.1 M, pH 11.5, $I = 0.44$ M) at 25 $^\circ\text{C}$. The alkaline hydrolysis of the depsipeptide was stopped by diluting the reaction mixture (10 μ L) with HCl (0.1 M (aq), 290 μ L), and then, the solution was analyzed by UPLC with a detection wavelength of $\lambda = 220$ nm (Fig. S4 and S5). The obtained UPLC peaks were integrated at each eluted time, and the peak area was plotted versus time. The stability of the peptide is greatly enhanced upon binding with copper ions.

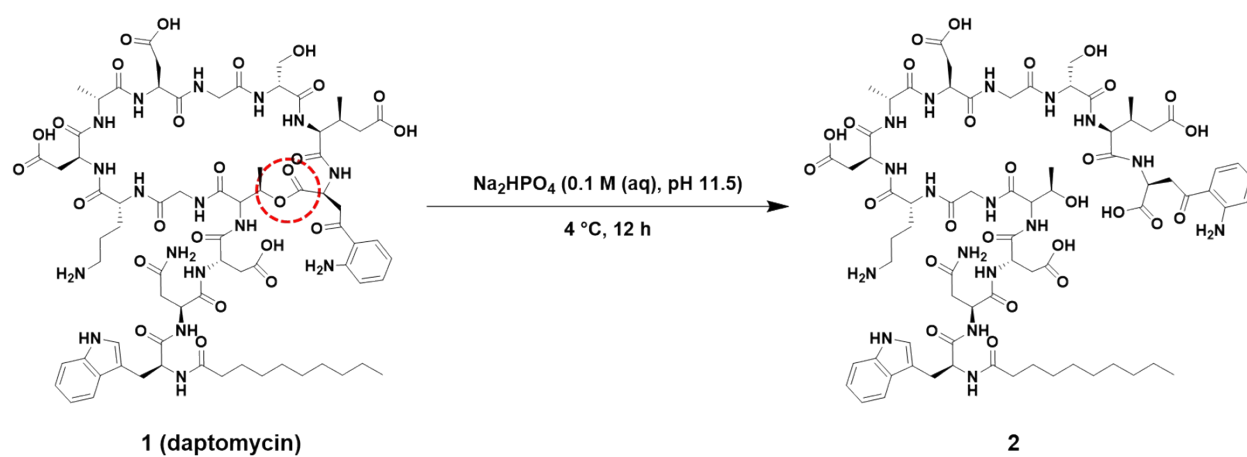


Figure S3. Hydrolysis of daptomycin in alkaline conditions.

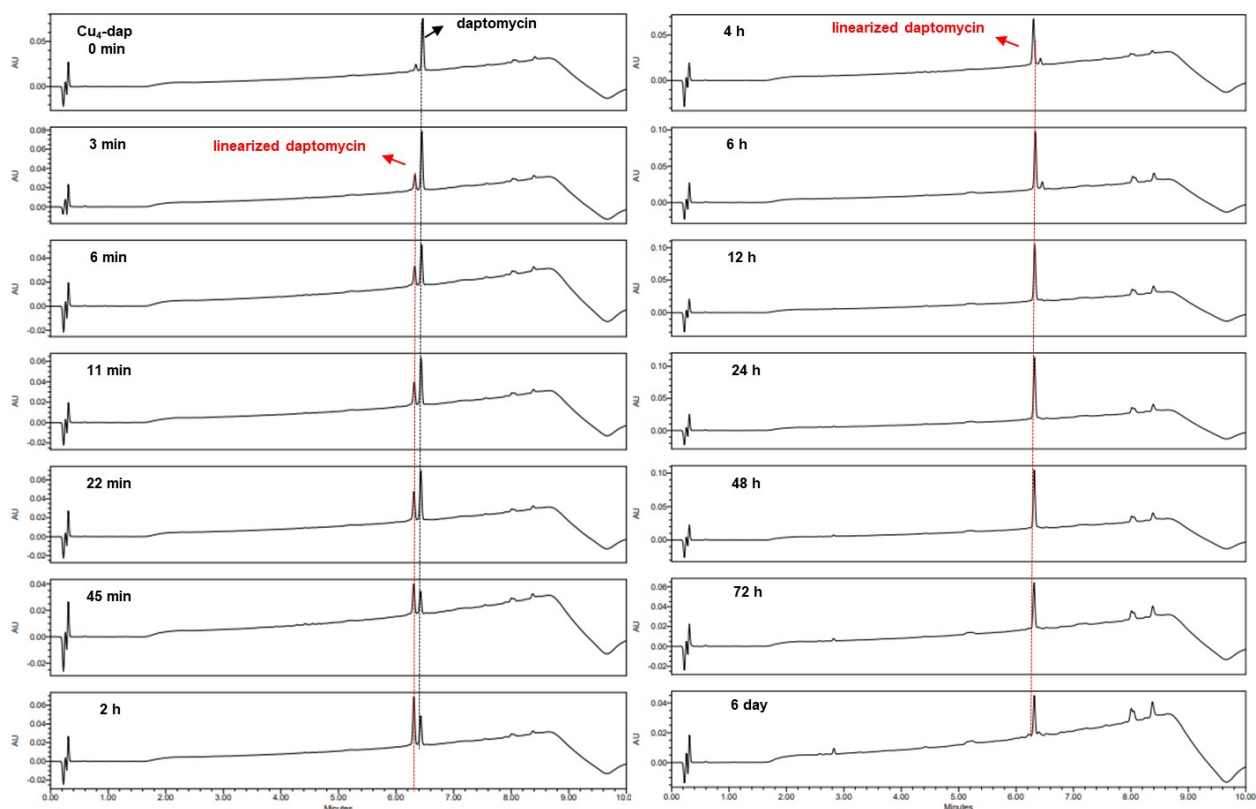


Figure S4. UPLC traces of daptomycin in the presence of 4 equiv of Cu(II). Daptomycin (**1**, $t_R = 6.3$ min) and linearized daptomycin (**2**, $t_R = 6.4$ min) were observed with UPLC at $\lambda = 220$ nm (see page S5 for the UPLC mobile phase conditions).

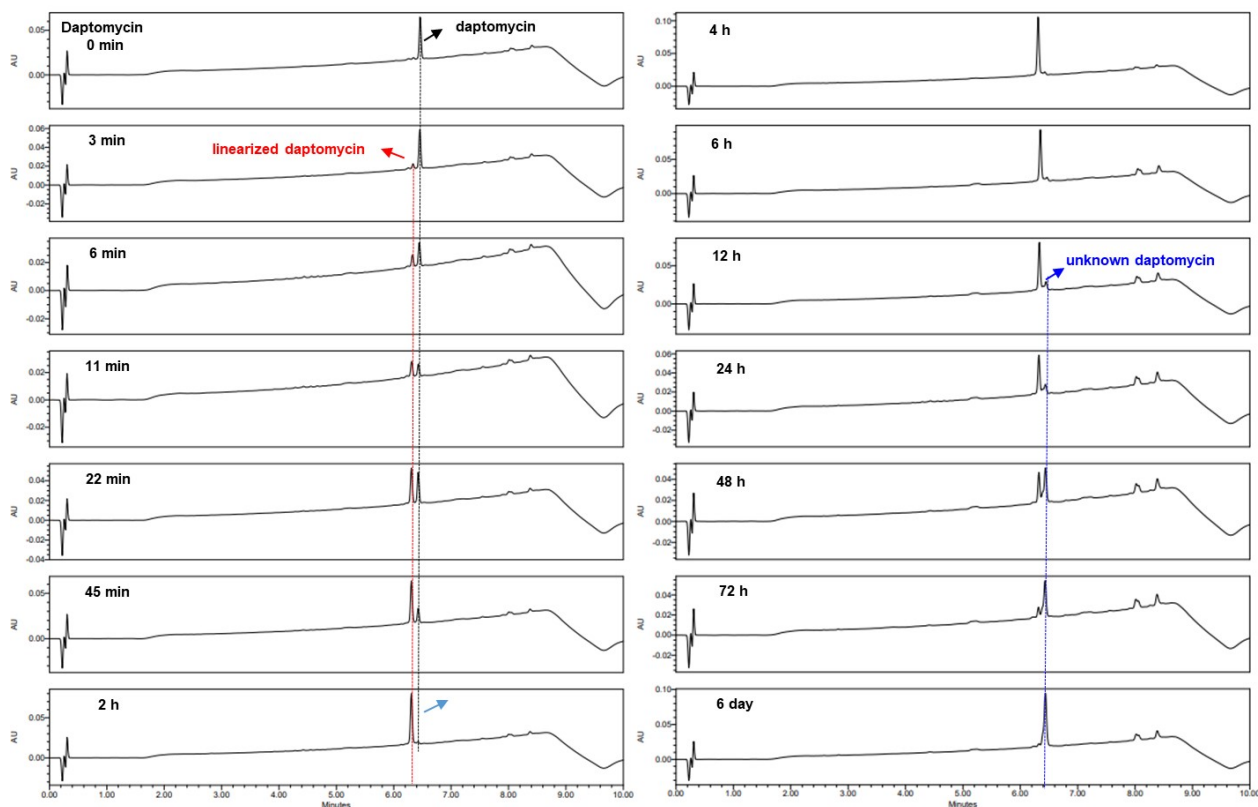


Figure S5. UPLC traces of daptomycin without Cu(II). Daptomycin (**1**, $t_R = 6.4$ min), linearized daptomycin (**2**, $t_R = 6.3$ min), and an unknown degradation product ($t_R = 6.4$ min) were observed with UPLC at $\lambda = 220$ nm (see page S5 for the UPLC mobile phase conditions).

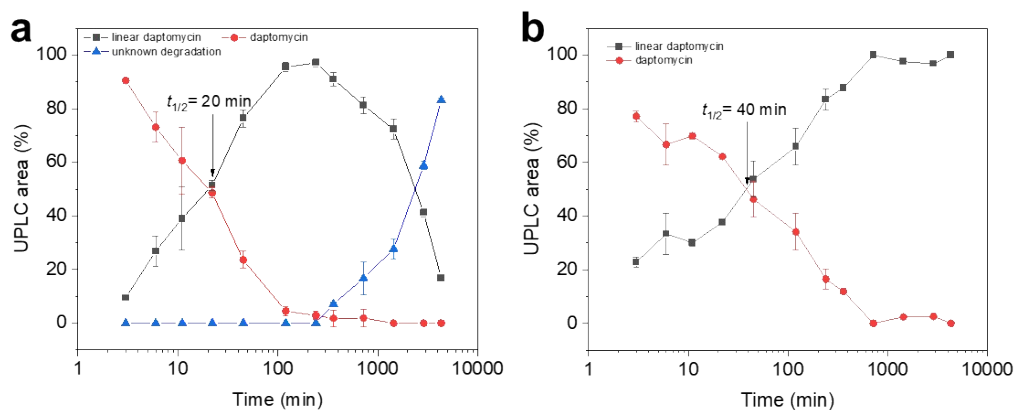


Figure S6. Kinetic study of daptomycin linearization. Ratio (%) of UPLC peak area at each retention time was plotted versus time: (a) without Cu(II) and (b) with 4 equiv of Cu(II). Error bars indicate the standard deviation from three independent experiments.

7. ESI-HRMS analysis of Cu_n-dap complexes

Samples for ESI-HRMS containing daptomycin (1 mM) and CuCl₂ (1–4 mM) were prepared by adjusting pH up to 11.5 with concentrated NH₄OH (aq) at 25 °C. The prepared Cu_n-dap (n = 1–4) samples were injected to a LTQ Orbitrap XL mass spectrometer (ThermoFisher Scientific, MA, USA) with a flow rate of 20 μL/min. The mass was detected in negative ion mode. The mass data analysis including isotope simulation was carried out using

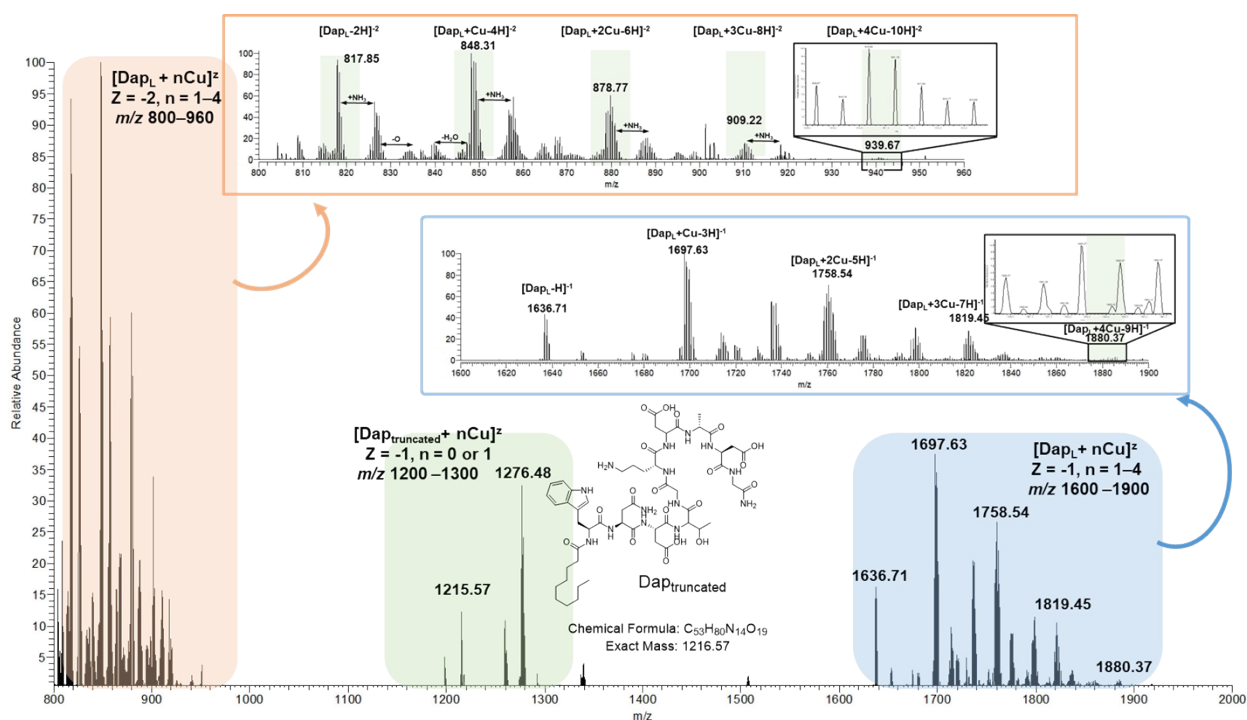


Figure S7. ESI-HRMS data of Cu₄-dap complex. Dap_L and Dap_{truncated} indicate linearized daptomycin and truncated peptide, respectively, in negative ion mode. In the range of 1600 – 1900 m/z, distinct peaks are assigned as the following species: 1636.71 [Dap_L-H]⁻¹, 1697.63 [Dap_L+Cu-3H]⁻¹, 1758.54 [Dap_L+2Cu-5H]⁻¹, 1819.45 [Dap_L+3Cu-7H]⁻¹, and 1880.37 [Dap_L+4Cu-9H]⁻¹.

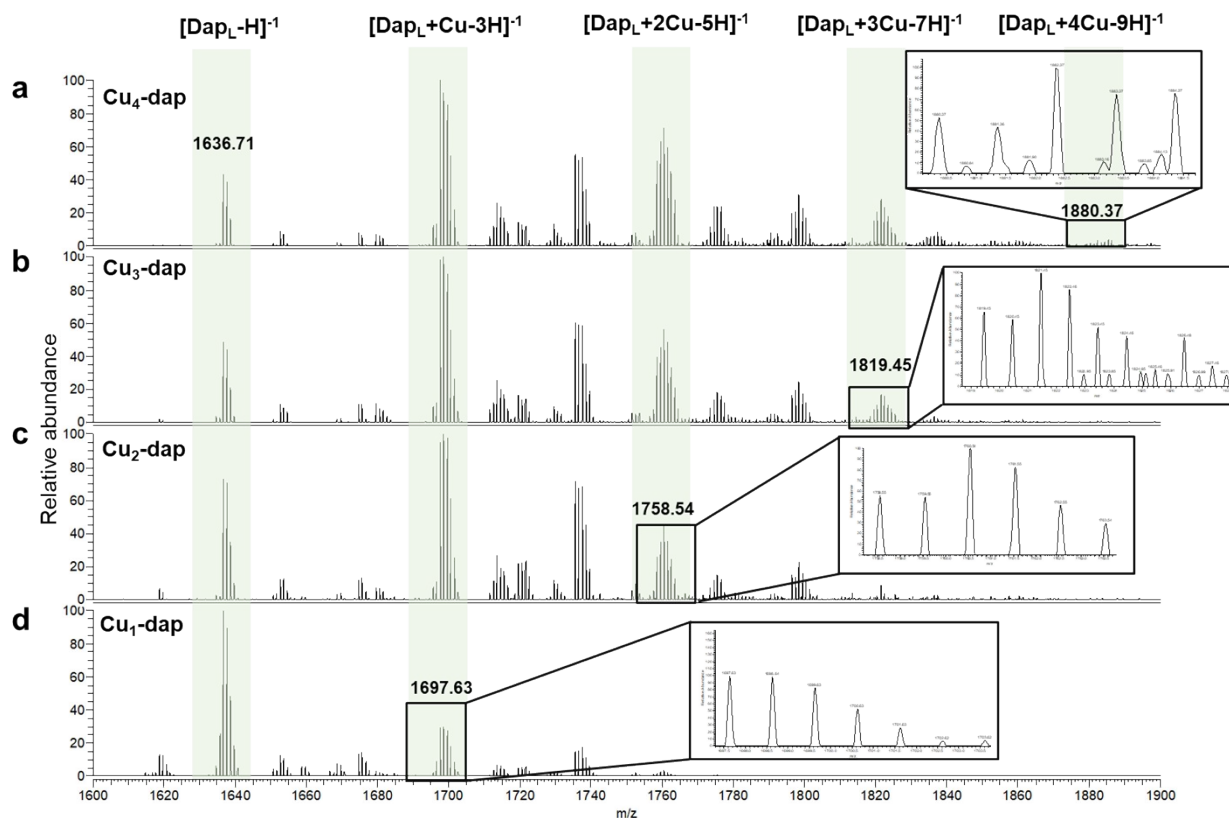


Figure S8. ESI-HRMS data of singly charged negative species of $\text{Cu}_n\text{-dap}$ ($n = 1-4$) complexes in the range of 1600-1900 m/z . Each mass spectrum was obtained by injection of (a) $\text{Cu}_1\text{-dap}$, (b) $\text{Cu}_2\text{-dap}$, (c) $\text{Cu}_2\text{-dap}$, and (d) $\text{Cu}_4\text{-dap}$ (1 mM in H_2O , pH 11.5, titrated with NH_4OH solution).

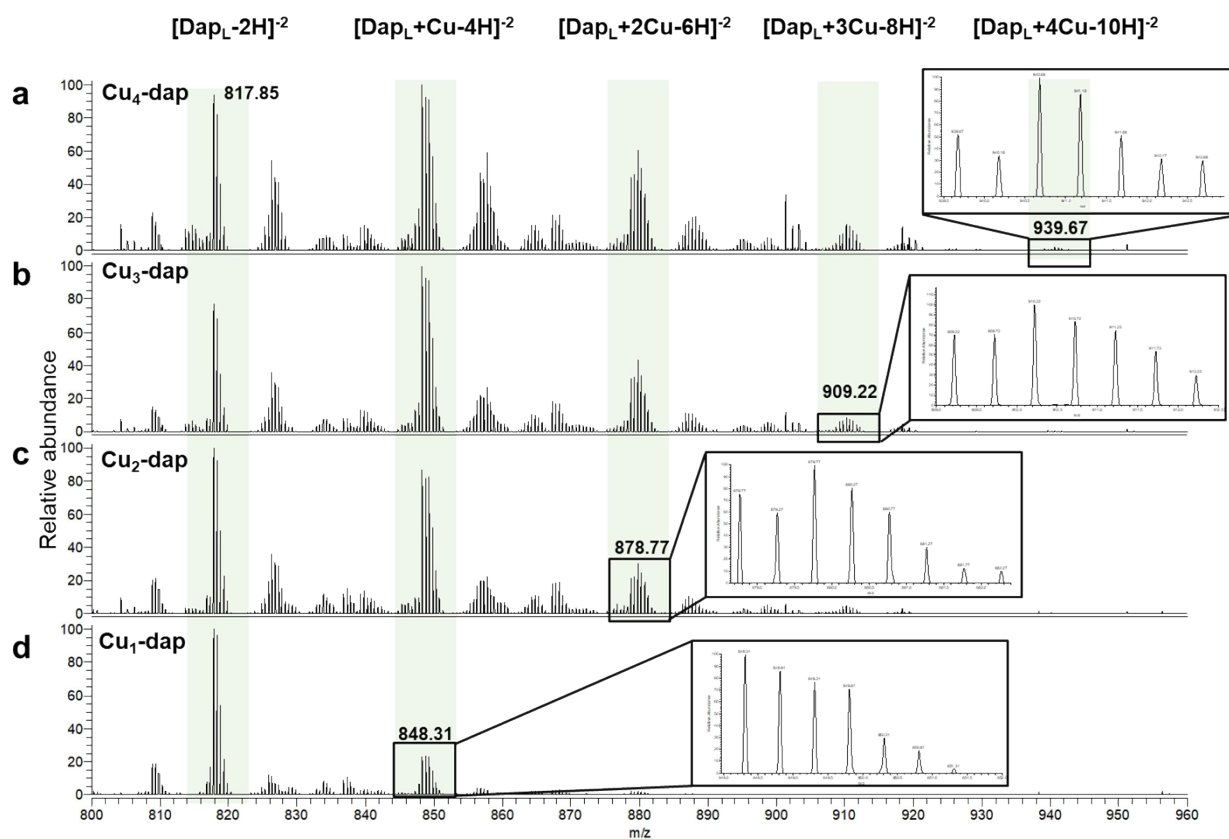


Figure S9. ESI-HRMS data of doubly charged negative species of $\text{Cu}_n\text{-dap}$ ($n = 1\text{--}4$) complexes in the range of 800-960 m/z . Each mass spectrum was obtained by injection of (a) $\text{Cu}_1\text{-dap}$, (b) $\text{Cu}_2\text{-dap}$, (c) $\text{Cu}_2\text{-dap}$, and (d) $\text{Cu}_4\text{-dap}$ (1 mM in H_2O , pH 11.5, titrated with NH_4OH solution).

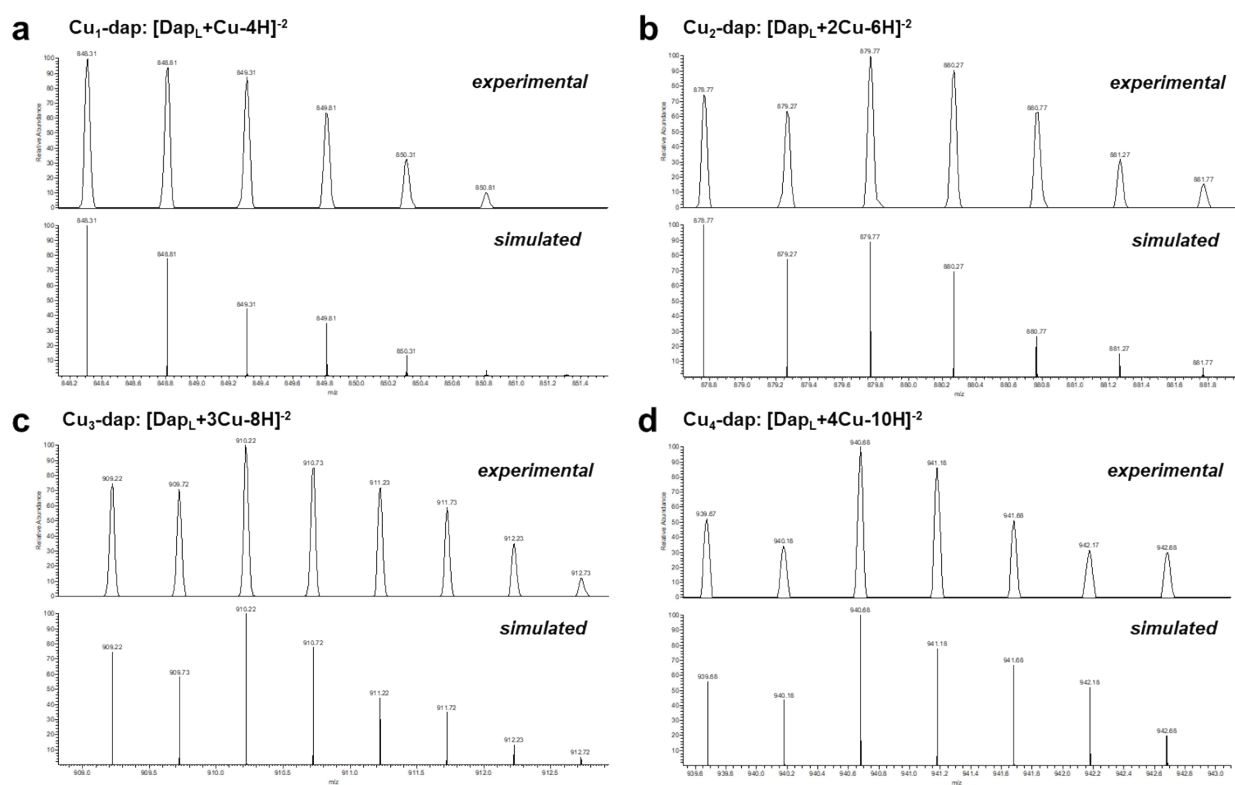


Figure S10. ESI-HRMS analysis of $\text{Cu}_n\text{-dap}$ ($n = 1\text{--}4$) complexes. The observed (top) and simulated isotopic patterns (bottom) for each mass spectrum of doubly charged negative ions: (a) $\text{Cu}_1\text{-dap}$, (b) $\text{Cu}_2\text{-dap}$, (c) $\text{Cu}_2\text{-dap}$, and (d) $\text{Cu}_4\text{-dap}$. The simulated isotopic patterns were obtained using Xcalibur software (ThermoFisher Scientific, MA, USA).

8. Electron paramagnetic resonance (EPR) spectroscopy

8.1. Continuous wave (CW)-EPR spectroscopy

For EPR spectroscopy, Cu_n-dap complexes (1 mM in Na₂HPO₄ buffer (0.08 M) with 20% glycerol) were prepared following the procedure described below. All the EPR measurements were carried out at the Western Seoul Center, Korea Basic Science Institute (KBSI) in Seoul, Korea. The CW X-band (9.6 GHz) EPR spectra were collected using a Bruker EMX plus 6/1 spectrometer equipped with an Oxford Instrument ESR900 liquid He cryostat using an Oxford ITC 503 temperature controller. All the spectra were collected with the following experimental parameters: microwave frequency, 9.6 GHz; microwave power, 0.05 mW; modulation frequency, 100 kHz; modulation amplitude, 10 G; time constant, 40.96 ms; 2 scans; temperature, 20 K.

8.2. Pulse EPR spectroscopy

Q-band (33.9 GHz) pulse EPR data were obtained on a Bruker Elexsys E580 spectrometer using an EN5107D2 resonator and Cryogenic temperatures were achieved with an Oxford CF-935 cryostat and Oxford ITC temperature controller. The measurements were conducted at 15 K. The ESE-EPR spectra were acquired using a pulse sequence, $\pi/2$ - τ - π -echo, with a pulse length $t_{\pi/2} = 32$ ns, $t_{\pi} = 64$ ns and $\tau = 200$ ns. The Davies electron nuclear double resonance (ENDOR) were performed using the π - T - $\pi/2$ - τ - π -echo, with microwave pulse lengths of $t_{\pi/2} = 32$ ns, $t_{\pi} = 64$ ns and an inter-pulse time of $\tau = 200$ ns. In this sequence, the RF power was applied during the time T (20 μ s) to drive nuclear spin transitions. The repetition time was 5 ms. The Mims ENDOR were performed using the $\pi/2$ - τ - $\pi/2$ - T - $\pi/2$ -echo, with microwave pulse lengths of $t_{\pi/2} = 32$ ns and an inter-pulse time of $\tau = 200$ ns. In this sequence, the RF power was applied during the time T (20 μ s) to drive nuclear spin transitions. The repetition time was 2 ms. All ENDOR spectra were collected by stochastic sampling for a better baseline of the spectra. All simulations of the EPR spectra were performed using Easyspin.³

8.3. Analysis of EPR spectra

The X-band continuous wave (CW) EPR of Cu_n-dap (Figures 2c and S11) displays an axial signal and the Q-band electron spin echo (ESE)-detected EPR spectrum shows the corresponding g tensor, $g = [2.198, 2.041, 2.041]$ (Figure S12). In the g_{\parallel} , the signal with the hyperfine coupling of Cu($I=3/2$) $A_{\parallel}(\text{Cu})$ presents ~ 590 MHz. The most apparent feature of the spectrum is a superhyperfine structure of ligand, which is characterized by nitrogen nuclei (^{14}N , $I=1$). In the g_{\perp} , the splitting of nine lines can be assigned to an equivalent of 4 nitrogens ($2*n*I+1$, $n=4$), where the averaging splitting is ~ 17 G, also confirmed by 33.9 GHz field-dependent ^{14}N ENDOR (Figure S14). In g_{\parallel} , the triplet ENDOR pattern of the spectrum can be assigned to the overlapped doublets that are centered at $A/2$ (21 MHz) and separated by $3P$ (6 MHz) and twice the ^{14}N Larmor frequency (7 MHz). In the simulations of the ENDOR spectra, the hyperfine coupling parameters of nitrogens were obtained $A(^{14}\text{N}) = [17.0, 14.5, 14.5]$ G and it is simultaneously well-matched on the CW-EPR. From overall multi-frequency/pulsed EPR results, it was characterized that the 4 equivalent nitrogens are coordinated to the central Cu(II) ion in the local geometries of the Cu_n-dap.

33.9 GHz ENDOR measurements were performed with Cu_n-dap ($n = 1$ and 4) solution prepared in H₂O and D₂O to investigate the proton of the axially coordinated ligand. The ^1H Davies ENDOR spectra of Cu₄-dap in H₂O show several doublets centered at the ^1H Larmor frequency with a hyperfine coupling constant of ~ 10 MHz (Figure S15). ^1H Davies ENDOR measurements of the sample prepared in D₂O were also conducted to examine whether an exchangeable proton was present (Figure S16). The ENDOR peak of the weakly coupled proton signal with ~ 5 MHz was decreased, which indicated that these peaks arise from the exchangeable proton. ^2H Mims ENDOR measurements of D₂O were further carried out to confirm the exchangeable proton. Noticeable doublet features centered at the ^2H Larmor

frequency are shown on the ^2H Mims ENDOR spectra with $A(^2\text{H}) \sim 1$ MHz. The hyperfine coupling of ^2H Mims ENDOR signals matches the difference in the ^1H Davies ENDOR signal scaled by a gyromagnetic ratio ($\nu_{\text{H}}/\nu_{\text{D}}$) of 6.51. In further analysis of the field-dependent ^2H Mims ENDOR experiments with exchangeable deuterium (Figure S15b), the detailed hyperfine coupling parameters were obtained with a tensor of ^2H , $A(^2\text{H}) = [-0.6, 1.5, 1.5]$ MHz with the Euler angle of $[\alpha, \beta, \gamma] = [0, 0, -]^\circ$ in the g-tensor frame, which indicated that the proton was positioned perpendicular to the plane. These features of the exchangeable proton were also shown in $\text{Cu}_1\text{-dap}$ and $\text{Cu}_4\text{-dap}$, which explains that the exchangeable proton was axially bound to each Cu of $\text{Cu}_n\text{-dap}$, and expected to be OH or H_2O from solvent media.

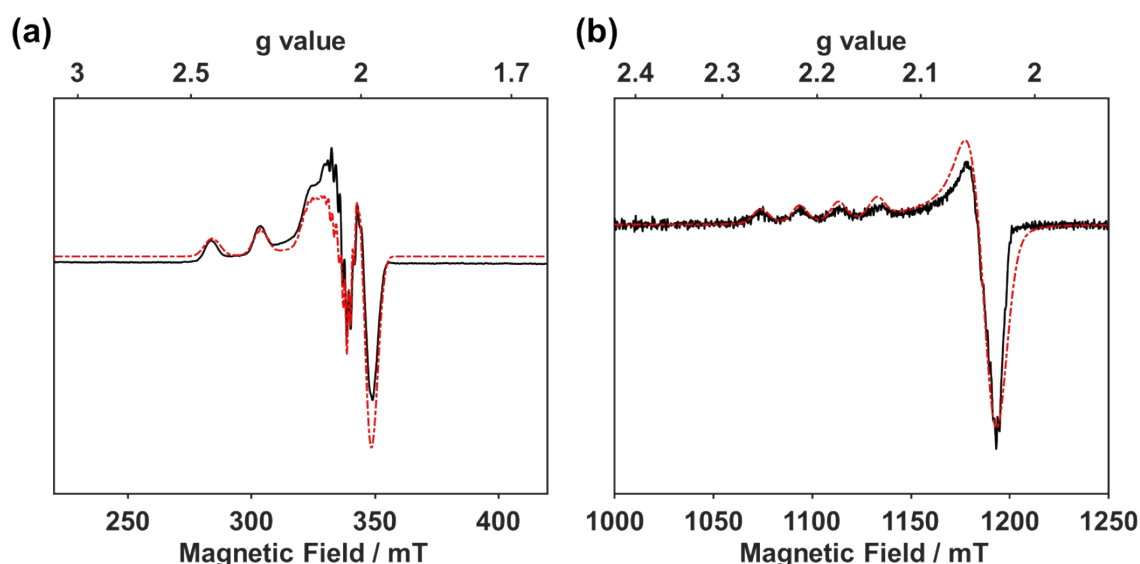


Figure S11. (a) 9.6 GHz CW-EPR and (b) 33.9 GHz ESE-EPR (derivative) spectra of $\text{Cu}_4\text{-dap}$ (black lines) and the simulated spectra (red dashed lines). Experimental parameters: (a) Microwave frequency, 9.6 GHz; microwave power, 0.05 mW; modulation frequency, 100 kHz; modulation amplitude, 10 G; time constant, 40.96 ms; 2 scans; temperature, 20 K. (b) Microwave frequency, 33.9 GHz; pulse sequence, 32-64 ns; inter-pulse time (τ), 400 ns; temperature, 20 K. Simulation parameters: $g = [2.198, 2.042, 2.042]$, $A(\text{Cu}) = [210, 30, 30]$ G, $A(^{14}\text{N}) = [17.0, 14.5, 14.5]$ G.

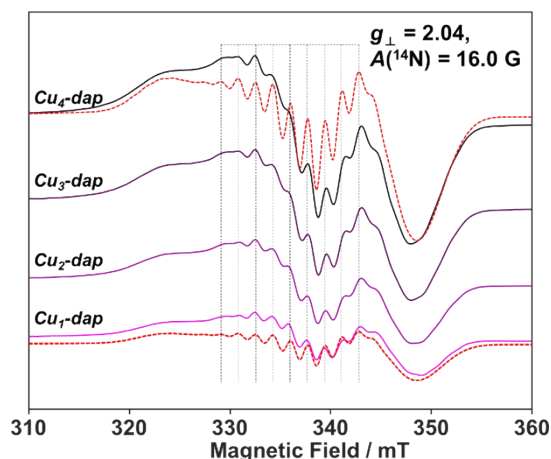


Figure S12. EPR spectra of $\text{Cu}_n\text{-dap}$ in the g_{\perp} region and the simulated spectra of $\text{Cu}_1\text{-dap}$ and $\text{Cu}_4\text{-dap}$ (red dashed lines). Experimental parameters: Microwave frequency, 9.6 GHz; microwave power, 0.05 mW; modulation frequency, 100 kHz; modulation amplitude, 10 G; time constant, 40.96 ms; 2 scans; temperature, 20 K. Simulation parameters: $g = [2.198, 2.042, 2.042]$, $A(\text{Cu}) = [210, 30, 30]$ G, $A(^{14}\text{N}) = [17.0, 14.5, 14.5]$ G.

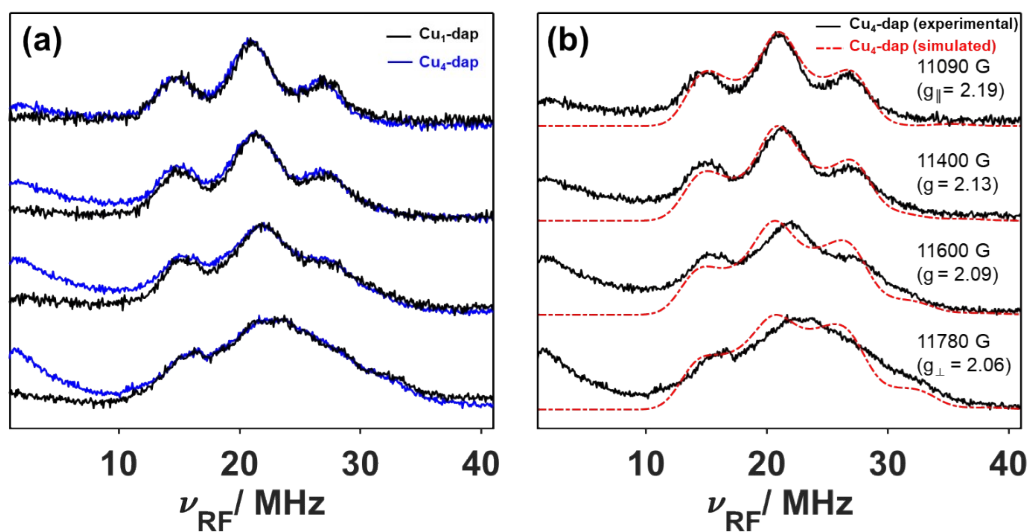


Figure S13. 33.9 GHz- ^{14}N Davies ENDOR of (a) $\text{Cu}_n\text{-dap}$ ($n = 1$ and $n = 4$), and (b) $\text{Cu}_4\text{-dap}$ and the simulated spectra of $\text{Cu}_4\text{-dap}$ (red dashed lines). Experimental parameters: Microwave frequency, 33.9 GHz; pulse sequence, 64-32-64 ns; inter-pulse time (τ), 200 ns; temperature, 15 K. Simulation parameters for (b): $g = [2.198, 2.042, 2.042]$, $A(^{14}\text{N}) = [17.0, 14.5, 14.5]$ G.

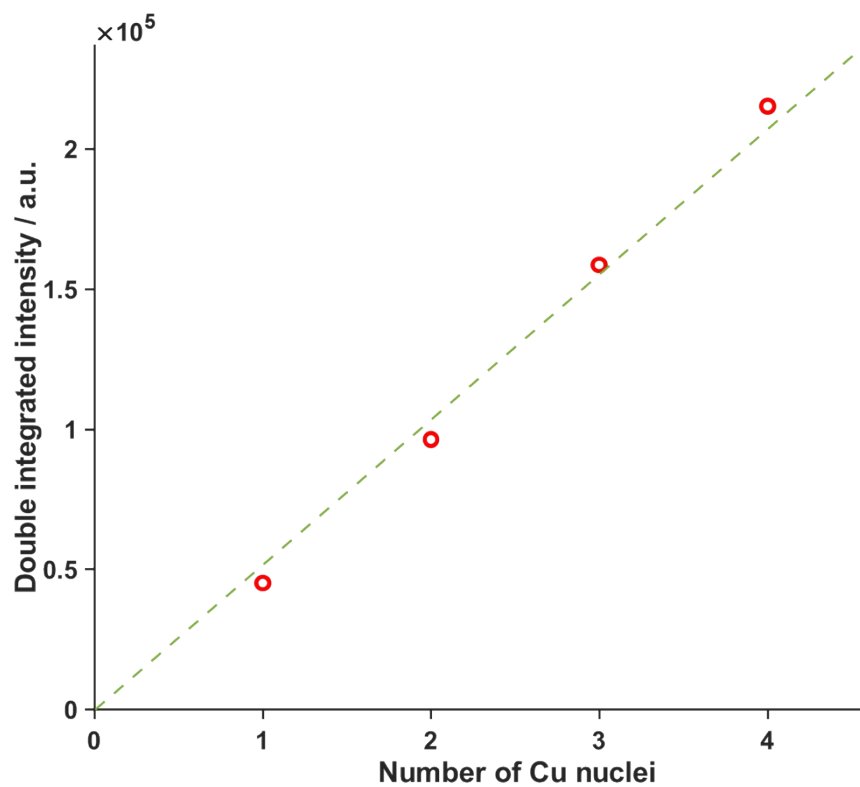


Figure S14. Double integrated intensity calculated from CW-EPR spectra (Figure 2c) plotted with the increasing number of copper ions in $\text{Cu}_n\text{-dap}$ ($n = 1\text{--}4$).

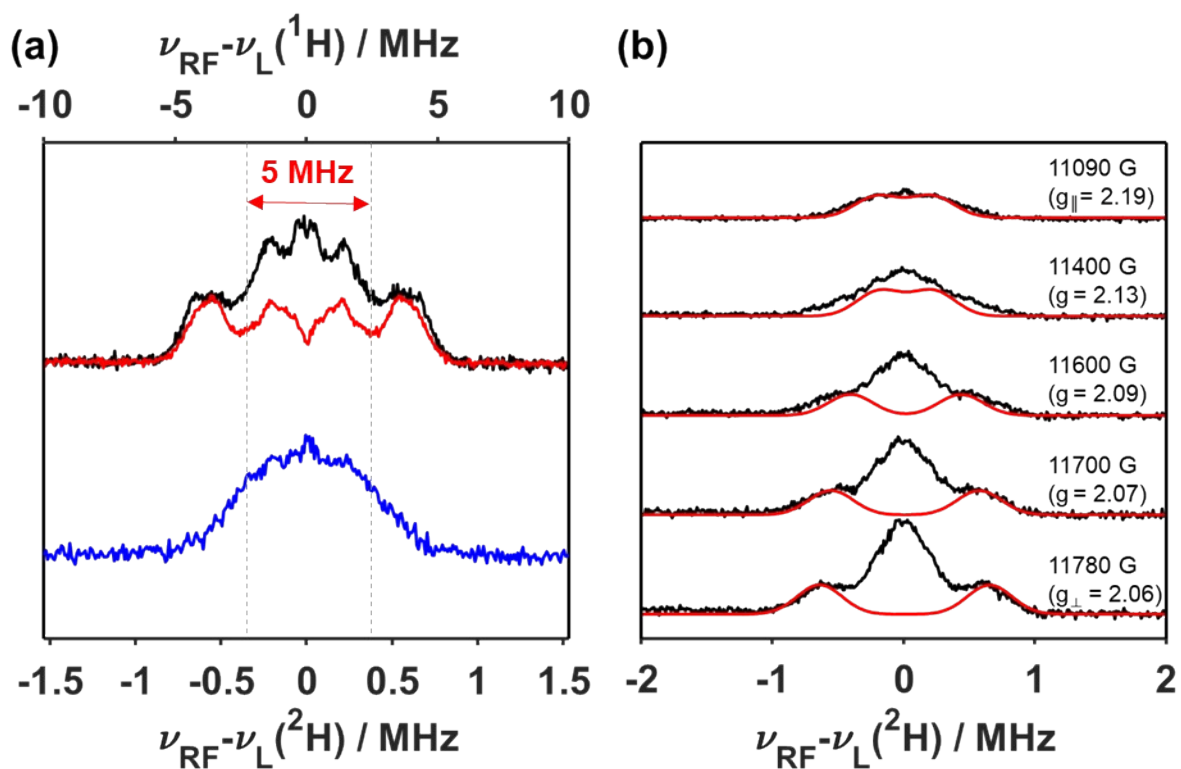


Figure S15. 33.9 GHz ^1H ENDOR spectra of $\text{Cu}_4\text{-dap}$. (a) ^1H Davies ENDOR of $\text{Cu}_4\text{-dap}$ in H_2O (black line), in D_2O (red line), and ^2H Mims ENDOR in D_2O (blue line) at g_{\parallel} . (b) Field dependent ^2H Mims ENDOR spectra of $\text{Cu}_4\text{-dap}$ (black lines) and the simulated spectra (red lines). Experimental parameters for ^1H Davies ENDOR (a): microwave frequency, 33.9 GHz; pulse sequence, 64-32-64 ns; inter-pulse time (τ), 200 ns; and temperature, 15 K. Experimental parameters for ^2H Mims ENDOR (a): microwave frequency, 33.9 GHz; pulse sequence, 32-32-32 ns; inter-pulse time (τ), 200 ns; and temperature, 15 K. Simulation parameters for (b): $g = [2.198, 2.042, 2.042]$, $A(^2\text{H}) = [-0.6, 1.5, 1.5]$ G.

9. Evans method

The Evans method measures the magnetic susceptibility (χ_M) using an NMR spectrometer (JEOL ECS400, JEOL Ltd., Tokyo, JP). We employ a procedure for Evans method, which is reported by Powers, T. M. with following modifications.² Cu_n-dap and daptomycin samples (6.67 mM) were prepared by dissolving lyophilized samples in Na₂HPO₄ buffer (0.1 M in D₂O/H₂O (50:1, v/v)) (50:1, v/v). The resulting pH* values were ranging from 11.81 to 11.88. Using centrifugation at 10,000 rpm over 5 min, any unbound Cu(II) was removed. Each sample (600 μ L) was transferred into NMR tube with capillary inset containing Na₂HPO₄ solution (0.1 M in D₂O/H₂O (50:1, v/v)), and ¹H NMR was recorded at 25 °C. The parameters on Table S2 were calculated from the obtained NMR spectra and Eq. S6–8.

Table S2. Evans method parameters for the number of unpaired electrons.

	δ_1 (ppm)	δ_2 (ppm)	Δf (Hz)	[Cu] (mM)	χ_M ($\times 10^{-3}$ cm ³ /mol)	μ_s	n_e
Linear dap	4.667	4.667	0	-	-	-	-
Cu ₁ -dap	4.669	4.633	14.400	6.667	1.290	1.754	1.019
Cu ₂ -dap	4.669	4.609	24.000	13.334	1.075	1.601	0.888
Cu ₃ -dap	4.669	4.577	36.800	20.001	1.099	1.619	0.903
Cu ₄ -dap	4.669	4.527	56.800	26.668	1.272	1.742	1.008

μ_s : magnetic moment, χ_M : molar magnetic susceptibility, T: temperature (K), δ_1 : pure solvent resonance, δ_2 : shifted resonance with paramagnetic species, F: spectrometer radio frequency in Hz (400 MHz), c: concentration of Cu(II) in solution (mol/mL), n_e : the number of unpaired electrons.

$$\Delta f = (\delta_1 - \delta_2) \times 400 \text{ MHz} \quad (\text{Eq. S6})$$

$$\chi_M = \frac{3\Delta f}{4\pi Fc} \quad (\text{Eq. S7})$$

$$\mu_s = \sqrt{8(\chi_M T)} \approx \sqrt{n_e(n_e + 2)} \quad (\text{Eq. S8})$$

10. Synthesis of the tetra-methyl ester derivative of daptomycin

The tetra-methyl ester derivative of daptomycin (tetra-methyl derivative) was synthesized according to the previously reported method by Miller and coworkers (Figure S16).⁴ Each crude peptide was purified by preparative HPLC and analyzed by analytical HPLC (Figure S17) and LC-MS.

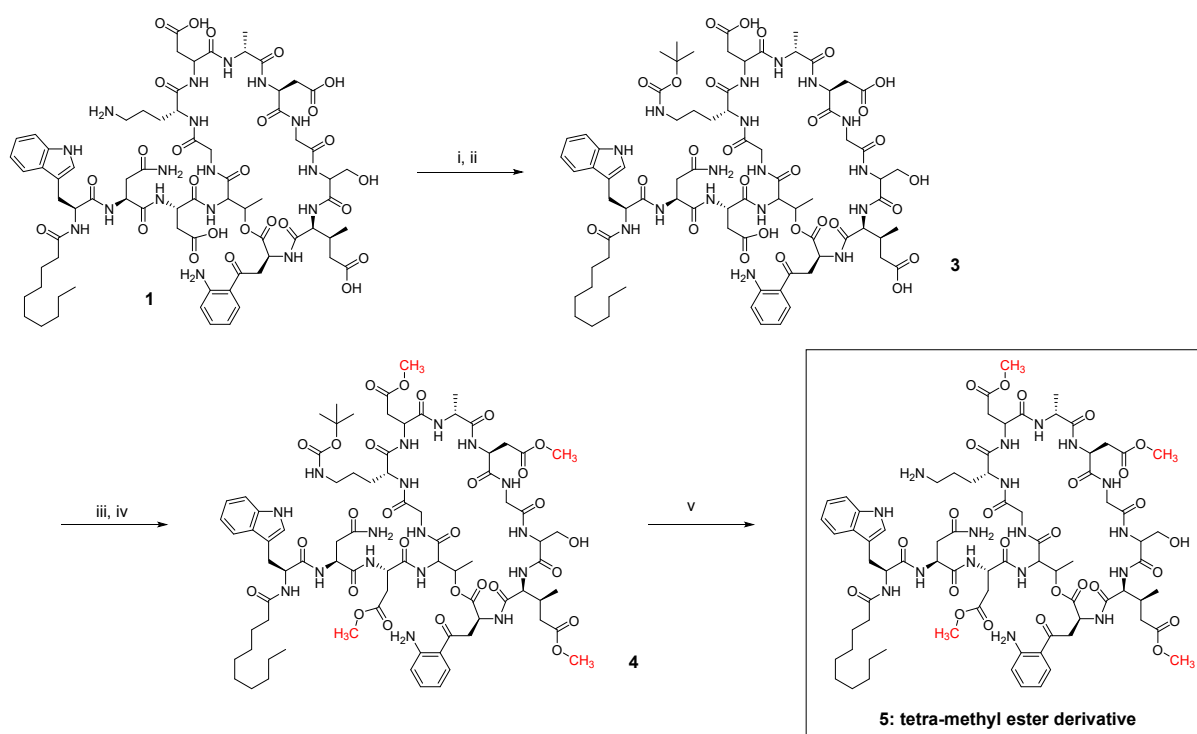


Figure S16. Synthetic procedure for preparing the tetra-methyl ester derivative of daptomycin.

(i) Boc_2O , pH 9–10, NaOH (aq), 0 °C to room temperature, 24 h; (ii) pH ~3, HCl (aq), 0 °C; (iii) pivalic anhydride, *i*-Pr₂NEt, 0 °C, 30 min; (iv) DMAP, MeOH, 0 °C, 30 min, ramp to room temperature, 6 h; (v) 50% TFA/CH₂Cl₂ (v/v), room temperature, 2.5 h.

10.1. Synthesis of Boc-protected daptomycin (**3**)

The pH of a stirring mixture of daptomycin (50 mg, 0.030 mmol, 1 equiv) in H₂O (1 mL) was adjusted to 10 by adding several drops of cold NaOH (1.0 M, aq) in an ice bath. Then, Boc₂O (17 mg, 0.077 mmol, 2.5 equiv) was added to the solution. The pH of the reaction mixture was readjusted to pH ~9 by addition of NaOH (1.0 M, aq). The reaction conversion was monitored using LC-MS, and the pH was kept to 9.0 at room temperature. After 24 h, the reaction mixture was acidified with cold HCl (1.0 M, aq) to pH ~3 in an ice bath, and the solvent was evaporated to afford a yellow solid. The crude product was dissolved in CH₃CN (1.0 mL) and purified using preparative HPLC with HPLC gradient **method 1** (see page S4). After purification, Boc-protected daptomycin (**3**) was obtained as a white powder (36 mg, 70% yield) *m/z* (LC-MS) calcd for C₇₇H₁₀₉N₁₇O₂₈ 1719.76, found 1720.7 [M+H]⁺.

10.2. Synthesis of the Boc-protected tetra-methyl ester derivative of daptomycin (**4**)

Pivalic anhydride (14 μL, 13 mg, 69 μmol, 7.9 equiv) was added to a stirring solution of **3** (14.9 mg, 8.7 μmol, 1.0 equiv) and *i*-Pr₂EtN (9.3 μL, 6.9 mg, 53 μmol, 6.1 equiv) in DMF (1.0 mL) at 0 °C and was stirred for 30 min. Then, DMAP (2.1 mg, 17 μmol, 2.0 equiv) and MeOH (0.10 mL, anhydrous) were added to the reaction mixture and stirred at 0 °C for 30 min. Then, the temperature was ramped to room temperature and stirred for 6 h. Using LC-MS, the conversion of the reaction was confirmed. The crude product was dissolved in 50% CH₃CN/H₂O (3.0 mL, v/v) and purified using preparative HPLC with HPLC gradient **method 2** (see page S4). After purification, the Boc-protected tetra-methyl ester derivative of daptomycin was obtained as a white powder (5.7 mg, 38% yield). *m/z* (LC-MS) calcd for C₈₁H₁₁₇N₁₇O₂₈ 1775.83, found 1777.7 [M+H]⁺.

10.3. Synthesis of the tetra-methyl ester derivative of daptomycin (5)

Protected peptide **4** (5.7 mg, 3.2 μmol) was dissolved in 50% TFA (1.0 mL) in anhydrous CH_2Cl_2 , and the reaction mixture was stirred for 2.5 h. Under blowing N_2 , the solvent was evaporated, and CH_2Cl_2 (~1 mL) was added to dissolve the product. The solvent was evaporated again to remove residual TFA. The crude peptide was dissolved in 50% $\text{CH}_3\text{CN}/\text{H}_2\text{O}$ (2.0 mL, v/v) and purified using preparative HPLC with HPLC gradient **method 2** (see page S4). The tetra-methyl ester derivative of daptomycin **5** (TFA salt) was obtained as a white powder (2.9 mg, 1.6 μmol (a TFA salt), 50% yield). m/z (LC-MS) calcd for $\text{C}_{77}\text{H}_{111}\text{N}_{17}\text{O}_{26}$ 1675.77, found 1676.8.

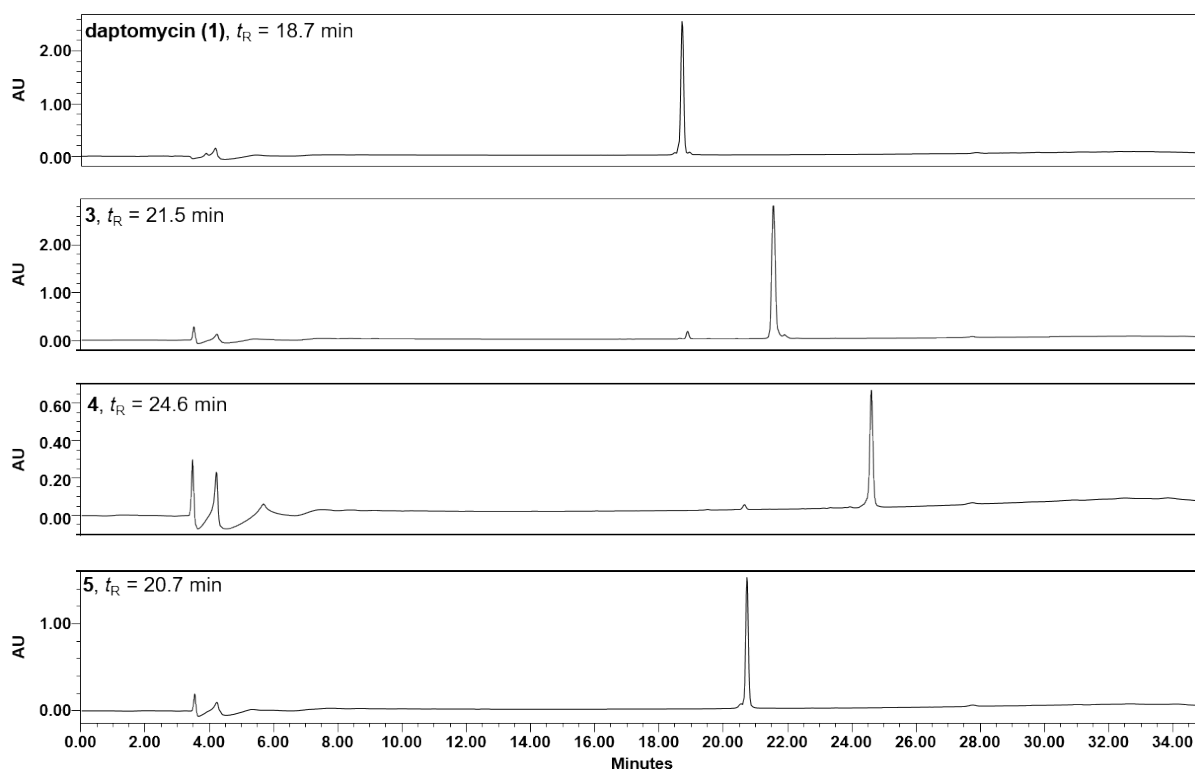


Figure S17. Analytical HPLC traces of the peptides purified with HPLC gradient **method 1** (see page S4).

11. Comparison between daptomycin and the tetra-methyl ester derivative **5** in metallation

For the kinetic study of Cu complexation with the peptides (daptomycin or tetra-methyl derivative **5**), to a solution of the peptide (1 mM, 1 mL) in Na₂HPO₄ buffer (0.1 M, pH 11.5, *I*=0.44 M) at 25 °C, 4 equiv of CuCl₂ (0.1 M (aq)) was added. The UV-vis spectra were recorded at the time points indicated (Figure S18).

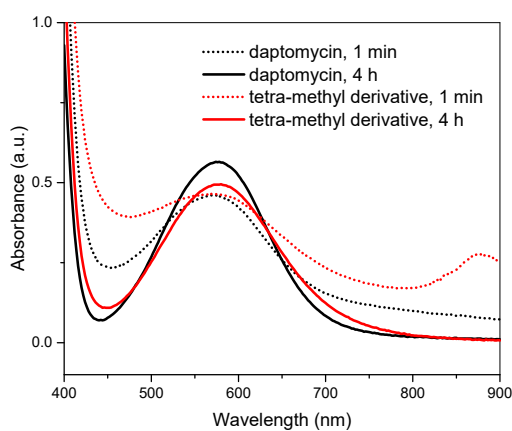


Figure S18. Kinetic study of metallation using daptomycin (**1**) or the tetra-methyl ester derivative of daptomycin (**5**). UV-vis spectra obtained at 1 min or 4 h after the addition of CuCl₂.

12. Cu(0/I/II) redox state assignment of Cu_n-dap complexes

To deconvolute the redox couples from the multiple redox signals, additional CVs were analyzed. A CV with a narrow potential window of 0.4–1.2 V_{RHE} showed a single redox reaction at *ca.* 0.8 V_{RHE} with a peak separation of 100 mV (Figure S19a). Since the initial Cu oxidation state in the complex was +2, this redox peak can be attributed to either that of Cu(I/II) or Cu(II/III). However, since the reported redox potential for Cu(II/III) is in 1.2–1.4 V_{RHE}, much higher than that of the Cu₄-dap complex, the observed redox couple is predicted to be Cu(I/II). It is consistent with the reported values for Cu(I/II) redox potential in 0.5–0.8 V_{RHE} (Table S3). Afterward, the CV study was carried out in 0.05–1.2 V_{RHE}, showing oxidation and reduction peaks at *ca.* 0.6 and 0.2 V_{RHE}, respectively. The new reduction peak at *ca.* 0.2 V_{RHE} is likely attributed to the Cu(II) and/or Cu(I) to Cu(0) reactions, which is consistent with reported values (Table S3). During these processes, the formed Cu(0) is supposed to be adsorbed on the GC substrate as discussed in other literatures, eventually inducing a heterogeneous process.⁵⁻⁷ We assume that this redox process likely involves demetallation of Cu(0 or I) and geometrical rearrangement of the Cu-complexes; therefore, the oxidation peak at 0.60 V_{RHE} possibly indicates the Cu(0) to Cu(I) and/or Cu(II) reactions accompanying re-complexation of Cu(II)/Cu(I) species with the peptide backbones. This heterogeneous process can account for the highly irreversible feature of the Cu(II/0 or I/0) redox reaction.

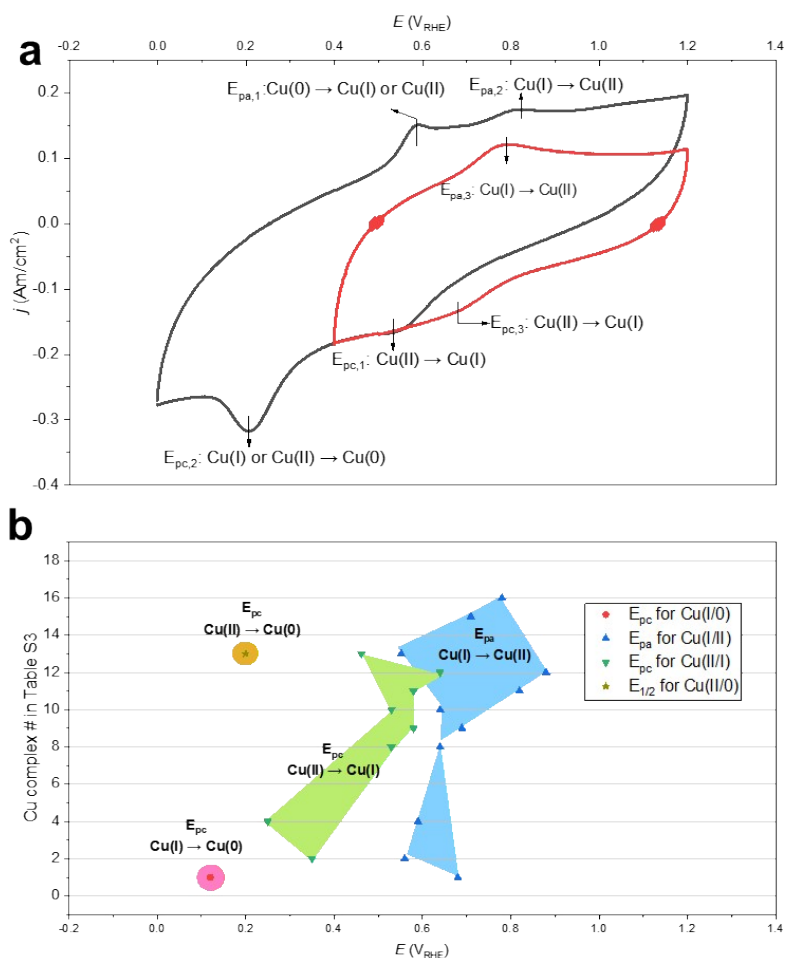
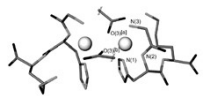
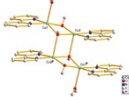

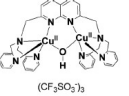
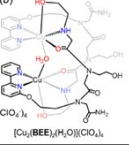
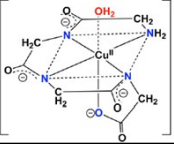
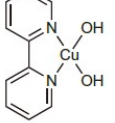
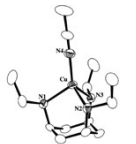
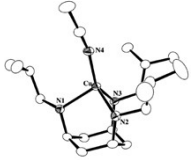
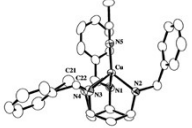
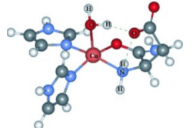
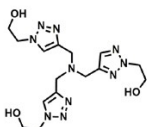
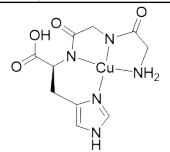
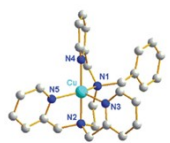
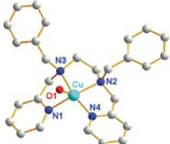
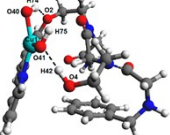


Figure S19. (a) CV results measured with $\text{Cu}_4\text{-dap}$ complex (1 mM) with different potential windows in a sodium phosphate buffer (0.1 M, pH 11.5, $I = 0.44$ M) at 25 °C. The electrochemical analyses were conducted with a potentiostat (VMP3, Bio-Logic Science Instruments, FR) and a rotating disk electrode instrument (RRDE-3A, ALS) in a two-compartment cell equipped with a graphite rod and an Ag/AgCl reference electrode (RE-16 for strong alkaline media, polyether ether ketone body (PEEK), EC-Frontier) as the counter and reference electrodes, respectively. A 5 mm-diameter glassy carbon (GC) rotating disk electrode was used as the working electrode after it was mirror polished with an alumina slurry (0.5 μm , R&B Inc., KR). (b) The reported potentials of Cu redox with various Cu molecular complexes (see Table S3 for the details in reported potentials).

Table S3. The previously reported redox potentials in CV analysis for Cu(II) complexes.

Cu complex	Cu sites	Nuclearity	Redox (E (V_{RHE}))					Ref
			Cu(I/0)	Cu(II/0)	Cu(II/I)	Cu(I/II)	Cu(II/III)	
	Cu-N ₃ O	1	0.12	nd	nd	0.68	nd	6
	Cu-N ₂ O ₃	4	nd	nd	0.35 (Cu ^{II} ₄ → Cu ^{II} ₃ Cu ^I)	0.56 (Cu ^{II} ₃ Cu ^I → Cu ^{II} ₄)	nd	8
	Cu-N ₄ O ₁	1	nd	nd	$E_{1/2} = 0.47 V_{\text{RHE}}$		nd	9
	Cu-N ₄ O	2	nd	nd	0.25 (Cu ^{II} ₂ → Cu ^{II} Cu ^I)	0.59 (Cu ^{II} Cu ^I → Cu ^{II} ₂)	nd	10
	Cu-N ₃ O ₃	2	nd	nd	$E_{1/2} = 0.6 V_{\text{RHE}}$		nd	11
	Cu-N ₄ O ₂	1	nd	nd	nd	nd	1.23	12
	Cu-N ₂ O ₂	1 or 2	nd	nd	$E_{1/2} = 0.64 V_{\text{RHE}}$		nd	13

8		Cu-N ₄	1	nd	nd	0.53 ^a	0.64 ^a	nd	14
9		Cu-N ₄	1	nd	nd	0.58 ^a	0.69 ^a	nd	14
10		Cu-N ₄	1	nd	nd	0.53 ^a	0.64 ^a	nd	14
11		Cu-A β Cu-N ₃ O ₂ ^b	1	nd	nd	0.58	0.82	nd	15, 16
12		nd	nd	nd	nd	0.64	0.88	nd	17
13		Cu-N ₄	1	nd	0.20	0.46	0.55	1.44	5, 18
14		Cu-N ₆	1	nd	nd	E _{1/2} = 0.56 V _{RHE}		nd	19

15		Cu-N ₄ O	1	nd	nd	nd	0.71	nd	19
17		Cu-N ₂ O ₂	1	nd	nd	0.48	0.78	0.98	20

^a The potentials were measured in 9:1 (v/v) CH₂Cl₂/MeCN vs. SCE. ^b adapted from as the Davies ENDOR EPR-based structure determination.¹⁶ ‘nd’ indicates the values were not determined.

13. Ascorbic acid oxidation

Ascorbic acid (Asc) oxidation with $\text{Cu}_n\text{-dap}$ ($n = 0\text{--}4$) was evaluated in Na_2HPO_4 buffer (0.1 M, pH 11.5, $I = 0.44$ M) by measuring the absorbance at 265 nm versus time at 25 °C.^{21, 22} The absorbance was measured using a TECAN microplate plate reader with a kinetic measurement mode which records the absorbance at 265 nm for 2 min. The final solution containing the Cu-peptide complex (1 μM , 200 μL) in the buffer with Asc (0.25 mM) was transferred to a quartz microplate (Hellma Analytics, Müllheim, GE). Based on the obtained absorbance of Asc solution versus concentration plot (3.53 abs/mM, Figure S20), the concentration during oxidation was calculated. By obtaining consumed Asc concentration for 2 min, the reaction rate was calculated. Since autoxidation of Asc in buffer solution was observed ($v_{o, \text{Asc ox}} = 0.43 \pm 0.0008$ mM/min), the background reaction rate was subtracted from the obtained initial rates to provide corrected reaction rates (Table S4).

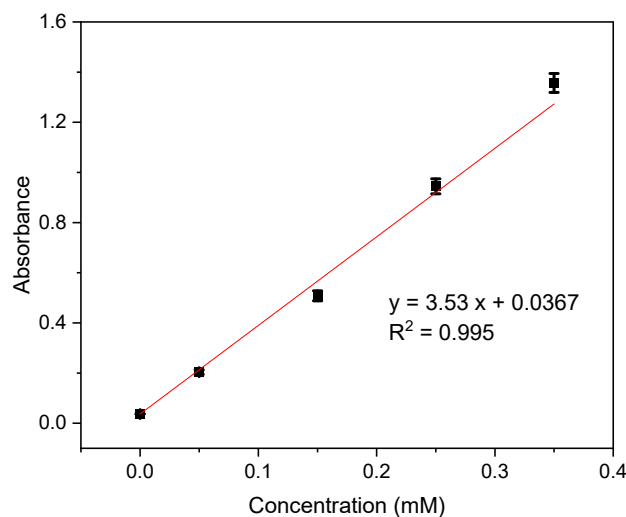


Figure S20. Absorbance at 265 nm was plotted along with Asc concentration in Na_2HPO_4 buffer (0.1 M, pH 11.5) at 25 °C. After triplicated experiments, the standard deviations were calculated and used for error bars.

Table S4. Results of Asc oxidation with Cu_n-dap and Cu-G₄.

	Corrected reaction rate (mM/min)
Blank	0
Linear dap	-0.0013 ± 0.0033
Cu ₁ -dap	0.0004 ± 0.0025
Cu ₂ -dap	0.0048 ± 0.0025
Cu ₃ -dap	0.0178 ± 0.0046
Cu ₄ -dap	0.0262 ± 0.0039
Cu ₈ -dap	0.0290 ± 0.0038
Cu-G ₄ ^a	0.0029 ± 0.0031

^a Cu-G₄ (4 μM) was used to maintain the same concentration of [Cu(II)] with Cu₄-dap (1 μM) in Na₂HPO₄ buffer (0.1 M, pH 11.5). After triplicated experiments, the averages and standard deviations were calculated.

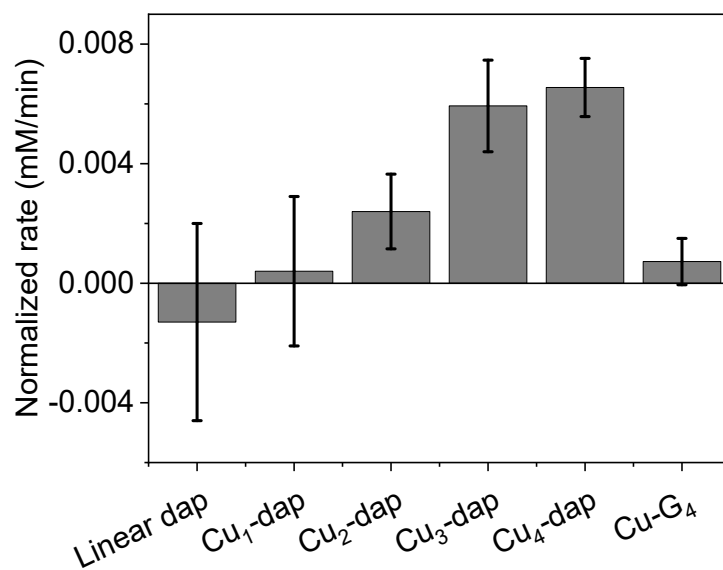


Figure S21. Normalized rate per the number of the bound Cu (II) for Asc oxidation mediated by Cu_n-peptide complexes. After triplicate experiments, the averages and standard deviations were calculated for each data point and error bar.

14. 2,6-Dimethoxyphenol oxidation

The catalytic activity of $\text{Cu}_n\text{-dap}$ for 2,6-dimethoxyphenol (DMP) oxidation was evaluated in a Na_2HPO_4 buffer (0.1 M, pH 11.5, $I = 0.44$ M) at 25 °C. The method previously reported by Makhlynets *et al.* was used with slightly modified conditions.²³ The absorbance was measured using a TECAN microplate plate reader with a kinetic measurement mode by recording the absorbance at 476 nm for 1 h. DMP stock solution (4 mM) was prepared by diluting 1.0 M DMP in isopropyl alcohol with Na_2HPO_4 buffer (0.1 M, pH 11.5). The final solution containing the Cu-peptide (5 μM , 200 μL) and DMP (1 mM) was transferred to a 96-well natural PP plate (Greiner BiO-One, Kremsmünster, AT). The obtained absorbance was changed to concentration by using the previously reported molecular extinction coefficient of 3,3',5,5'-tetramethoxybiphenol (14,800 $\text{cm}^{-1}\cdot\text{M}^{-1}$).⁵ The initial rate was acquired from the difference of initial absorbance and that after 3 min based on the Beer-Lambert law. The initial reaction rate of the background reaction ($v_{0, \text{DMP ox}} = 0.0508 \pm 0.0020$ $\mu\text{M}/\text{min}$) was subtracted from the obtained initial rates of the reactions that occurred with the Cu-peptide complexes to provide corrected reaction rates (Figures S22 and S23, Table S5).

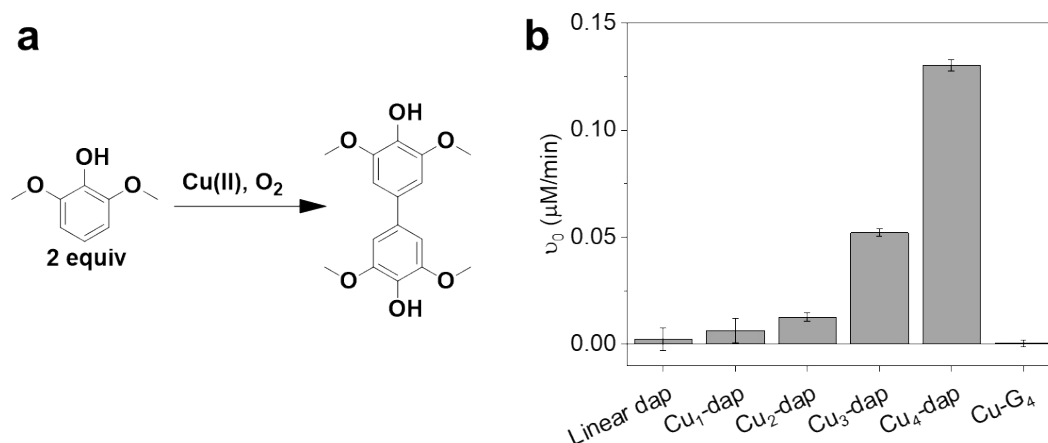


Figure S22. (a) DMP oxidation reaction. (b) Reaction rate of DMP oxidation with $\text{Cu}_n\text{-dap}$ (5 μM) and Cu-G₄ (20 μM). After triplicated experiments, the averages and standard deviations were calculated.

Table S5. Results of DMP oxidation with Cu_n-dap and Cu-G₄.

	Corrected reaction rate (μM/min)
Blank	0
Linear dap	0.0023 ± 0.0052
Cu ₁ -dap	0.0063 ± 0.0056
Cu ₂ -dap	0.0126 ± 0.0020
Cu ₃ -dap	0.0521 ± 0.0017
Cu ₄ -dap	0.1304 ± 0.0026
Cu-G ₄ ^a	0.0004 ± 0.0015

^aCu-G₄ (20 μM) was used to maintain the same concentration of [Cu(II)] with Cu₄-dap (5 μM) in Na₂HPO₄ buffer (0.1 M, pH 11.5). After triplicate experiments, the averages and standard deviations were calculated.

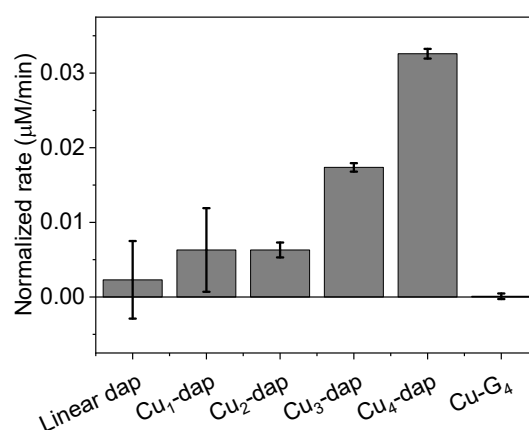


Figure S23. Normalized rate per the number of the bound Cu (II) for DMP oxidation mediated by Cu_n-peptide complexes. After triplicate experiments, the averages and standard deviations were calculated for each data point and error bar.

15. O₂ evolution measurement during H₂O₂ disproportionation with Cu_n-dap.

O₂ evolution was directly measured at 25 °C using a fiber-optic O₂ sensor (FireStingO₂, PyroScience, Aachen, GE) equipped with robust oxygen probe in a setup displayed on Figure S24. Using N₂ balloon, the atmosphere in reaction vessel containing Cu_n-dap solution (1 mM, 1 mL) was replaced with N₂, until the O₂ (%) value was stabilized. Then H₂O₂ (11.6 mM in Na₂HPO₄ buffer (0.1 M, pH 11.5, *I* = 0.44 M), 1 mL) was injected, and the O₂ (%) value was recorded. Using calibration curve obtained by direct injection of known O₂ moles in the same setup, the raw values (%) were converted to O₂ (moles) (Figure S25).

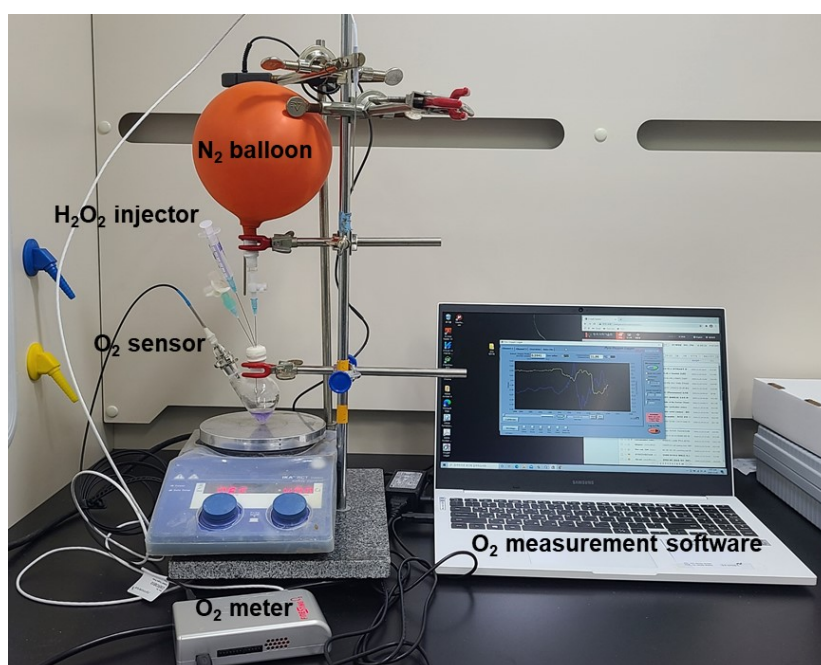


Figure S24. Experimental set up O₂ measurement of H₂O₂ disproportionation.

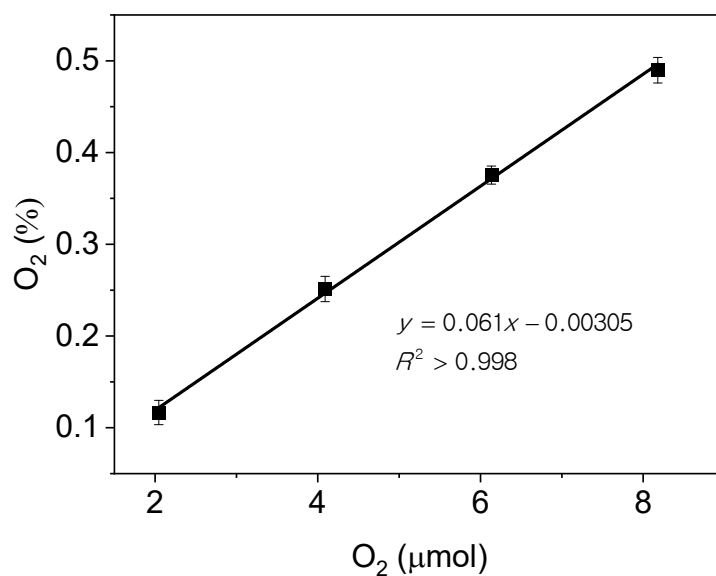


Figure S25. O₂ calibration curve to convert the read of the oxygen sensor (%) to the number of moles (μmol) measured in the reaction vessel. After triplicate experiments, the averages and standard deviations were calculated for each data point and error bar.

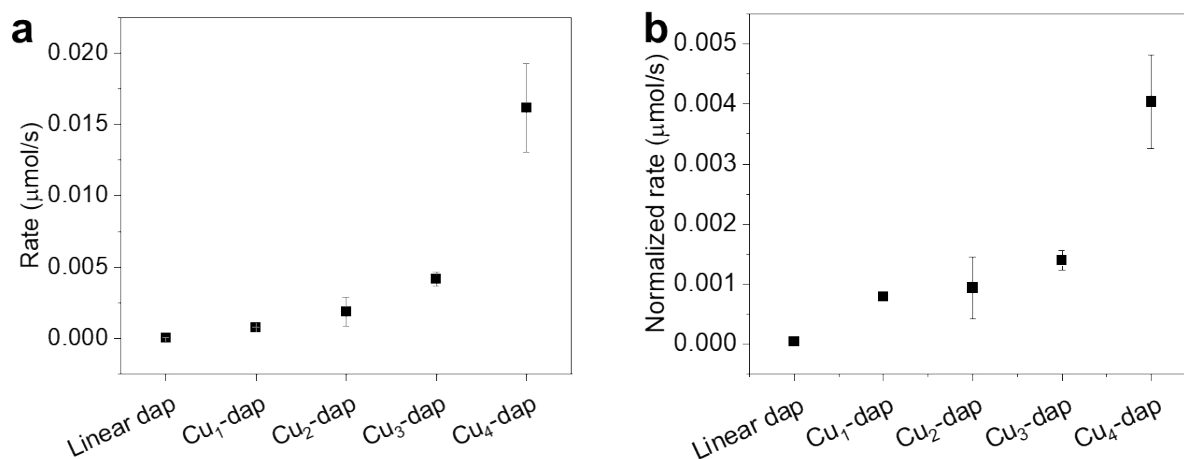


Figure S26. (a) Observed and (b) normalized rates per the number of the bound Cu (II) for H₂O₂ disproportionation mediated by Cu_n-dap complexes. After triplicate experiments, the averages and standard deviations were calculated for each data point and error bar.

16. Hydroxyl radical detection using 2,7-dichlorofluorescein diacetate

The hydroxyl radical was detected using 2,7-dichlorofluorescein diacetate (DCFH-DA) in Na_2HPO_4 buffer (0.1 M, pH 11.5, $I = 0.44$ M) at 25 °C with the Cu complexes (Figures S27).²⁴
²⁵ The emission at 535 nm with an excitation at 485 nm was measured using a Synergy H1 microplate plate reader with a kinetic measurement mode, which measures emission every 40 s. The final solution contained the Cu-peptide complex (1 μM , 200 μL) and DCFH-DA (10 μM) under four conditions; (1) no additives, (2) Asc (1 mM), (3) Asc (1 mM) and H_2O_2 (1 mM), and (4) H_2O_2 (1 mM). A PP black 96-well microplate (Greiner BiO-One, Kremsmünster, AT) was used. The intensity of the emission at 535 nm was measured three times for each condition (Figures S28 and S29, Table S6).

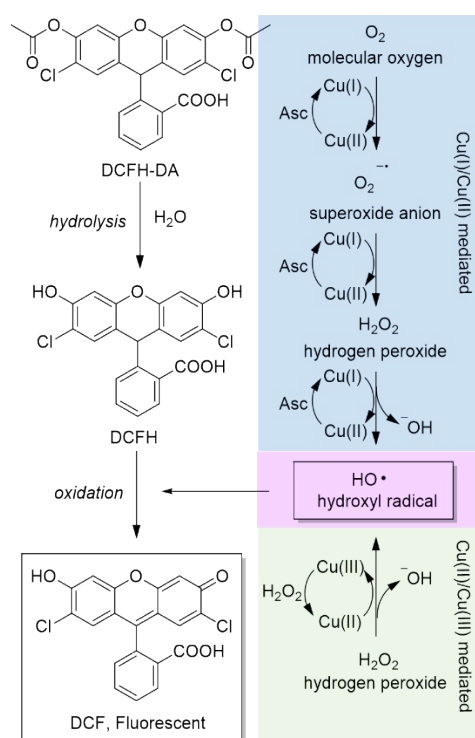


Figure S27. Conversion of DCFH-DA to DCF by hydroxyl radicals and two possible pathways for hydroxyl radical generation by copper catalysts.

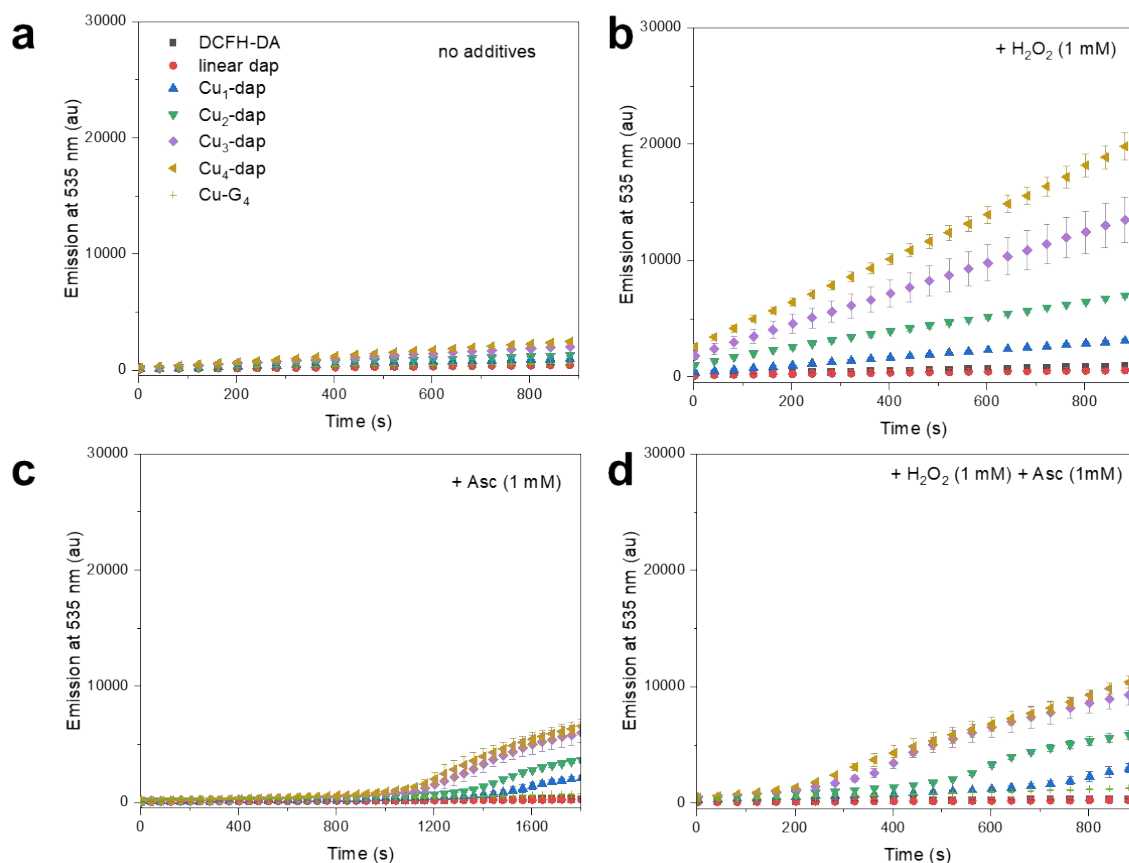


Figure S28. Emission at 535 nm versus time with/without Cu complexes (1 μ M): (a) with no additive, (b) with H₂O₂ (1 mM), (c) with Asc (1 mM), and (d) with Asc (1 mM) and H₂O₂ (1 mM). As shown in (c), there were two distinguishable emission increments of DCF in the presence of Asc. Slow \cdot OH generation at the earlier stage and subsequent rapid emission increase were observed. The two different stages suggest that Cu₄-dap generates \cdot OH through O–O bond cleavage of the accumulated H₂O₂ from the two-electron reduction of O₂ (see Figure S26). After triplicate experiments, the averages and standard deviations were calculated for each data point and error bar.

Table S6. Reaction rate of DCFH-DA oxidation with Cu_n-dap.

	Reaction rate (au/s)			
	No additive	+H ₂ O ₂	+Asc	+H ₂ O ₂ +Asc
Only DCFH-DA	0.447 ± 0.017	0.670 ± 0.018	0.142 ± 0.023	0.316 ± 0.010
Linear dap	0.331 ± 0.026	0.594 ± 0.042	0.138 ± 0.028	0.192 ± 0.020
Cu ₁ -dap	0.953 ± 0.047	3.055 ± 0.038	0.295 ± 0.024	1.307 ± 0.047
Cu ₂ -dap	1.244 ± 0.031	7.828 ± 0.104	0.248 ± 0.028	2.000 ± 0.034
Cu ₃ -dap	2.003 ± 0.033	13.746 ± 0.104	0.276 ± 0.023	3.169 ± 0.210
Cu ₄ -dap	2.331 ± 0.042	19.203 ± 0.245	0.345 ± 0.009	4.055 ± 0.221
Cu-G ₄ ^a	0.605 ± 0.017	0.966 ± 0.018	0.305 ± 0.020	1.382 ± 0.071

^aCu-G₄ (4 μM) was used to maintain the same concentration of [Cu(II)] with Cu₄-dap (1 μM) in Na₂HPO₄ buffer (0.1 M, pH 11.5, *I* = 0.44 M). The averages and standard deviations were calculated from the triplicate experiments.

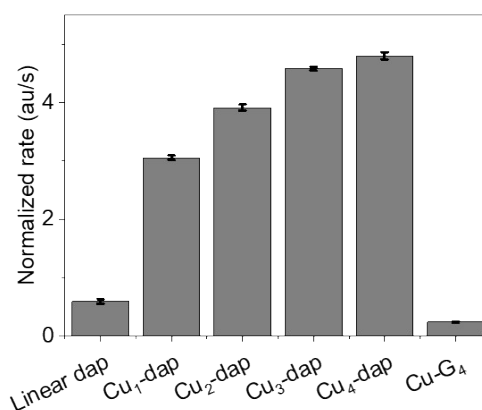


Figure S29. Reaction rate normalized by the number of the bound Cu (II) (au/s/the number of Cu) for ·OH generation mediated by Cu_n-dap complexes in the presence of H₂O₂. After triplicate experiments, the averages and standard deviations were calculated for each data point and error bar.

17. Electrochemical analysis

The electrochemical analyses were conducted with a potentiostat (VMP3, Bio-Logic Science Instruments, FR) and a rotating disk electrode instrument (RRDE-3A, ALS) in a two-compartment cell equipped with a graphite rod and an Ag/AgCl reference electrode (RE-16 for strong alkaline media, polyether ether ketone body (PEEK), EC-Frontier) as the counter and reference electrodes, respectively. To prevent glassware dissolution and halogen contamination, the cell was made of an acrylic plastic, and the working electrode was separated from the counter and reference electrodes by an ion-conducting membrane.^{26, 27} A 5 mm-diameter glassy carbon (GC) rotating disk electrode was used as the working electrode after it was mirror polished with an alumina slurry (0.5 μm , R&B Inc., KR).

In all the measurements, the Ar-saturated Na_2HPO_4 buffer (0.1 M, pH 11.5, $I = 0.44$ M) with and without $\text{Cu}_n\text{-dap}$ (1 mM, $n = 0\text{--}4$) was prepared with ultrapure water (> 18.2 M Ω , aqua MAXTM-Ultra 370 series, YOUNGLIN). The reference electrode was calibrated against a Pt electrode in the H_2 -saturated electrolyte, and all the potentials were reported in this study with respect to the reversible hydrogen electrode (RHE). Before the electrochemical analysis, the working electrode was first cleaned by 50 cycles of cyclic voltammetry (CV) in the potential range from 0.05 to 1.2 V_{RHE} with a 200 mV/s scan rate and in the blank Na_2HPO_4 buffer solution. Afterward, the working electrode was transferred to the Na_2HPO_4 buffer with $\text{Cu}_n\text{-dap}$ (1 mM, $n = 0\text{--}4$), and its polarization curve was measured with a 50 mV/s scan rate in the potential range from 0 to 1.2 V_{RHE} at 25 $^\circ\text{C}$. The oxygen evolution reaction (OER) was investigated by CV performed with a 5 mV/s scan rate for potentials ranging from 0 to 2 V_{RHE} and with a 1,600 rpm rotation rate.

Differential electrochemical mass spectrometry (DEMS) equipped with a scanning flow cell (SFC) combined with a mass spectrometer (Max 300 LG, Extrel, PA, USA), was used for the online gas product analysis at 25 $^\circ\text{C}$ (Figure S30). The SFC was equipped with U-shaped

electrolyte channels and had an opening diameter of 1 cm at the bottom of the cell, where the cell made electrical contact with the GC working electrode. A 1 mm tip covered with a porous Teflon membrane, through which gas and volatile products can evaporate into the vacuum system of the mass spectrometer, was located *ca.* 100 μm above the working electrode surface by controlling the thickness of the silicone sealing around the cell opening and the applied contact force. The contact between the SFC and working electrode and their distances were monitored by a digital microscope. An O_2 ($m/z = 32$) signal was detected during the OER measurement protocol performed with a 5 mV/s scan rate and in the potential range from 0 to 2 V_{RHE} .

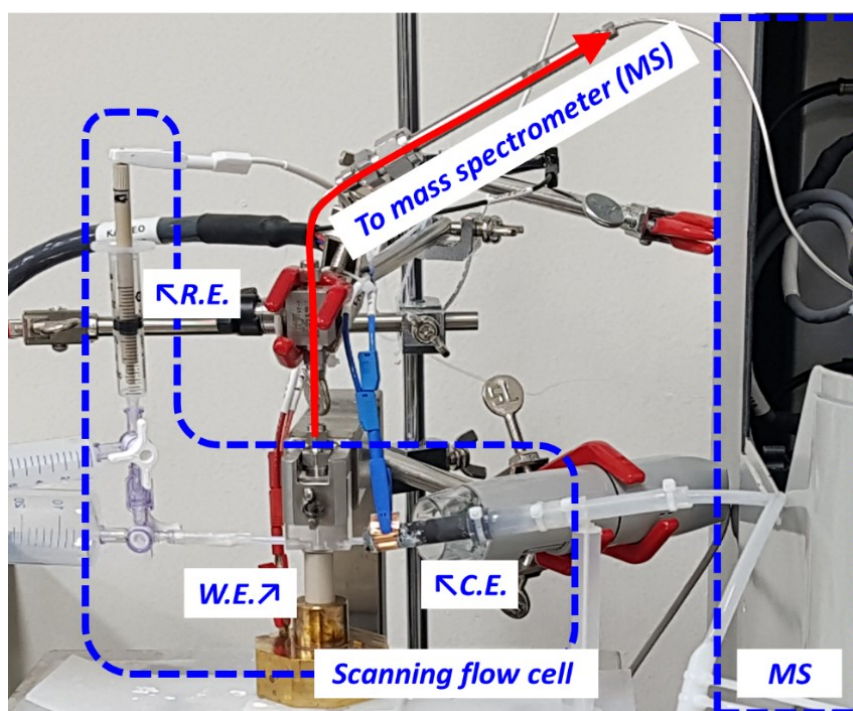


Figure S30. A digital photograph of the SFC/DEMS used in this study.

18. Differential pulse voltammetry (DPV)

Cu₄-dap solution (1 mM) prepared in Na₂HPO₄ buffer (0.1 M, pH 11.5, $I = 0.44$ M) was transferred to an electrolysis cell equipped with GC electrode ($S = 0.071$ cm²), Ag/AgCl (reference electrode), and Pt wire (counter electrode). The solution was thoroughly bubbled with N₂ to remove dissolved O₂. DPV measurement was carried out using CHI760E potentiostat (CH Instruments, Inc., TX, US) with the following parameters: Increment $E = 5$ mV, amplitude = 50 mV, pulse width = 0.05 s, sample width = 0.0167 s, pulse period = 0.5 s, quiet time = 2 s, sensitivity = 10^{-5} A/V, and temperature = 25 °C.

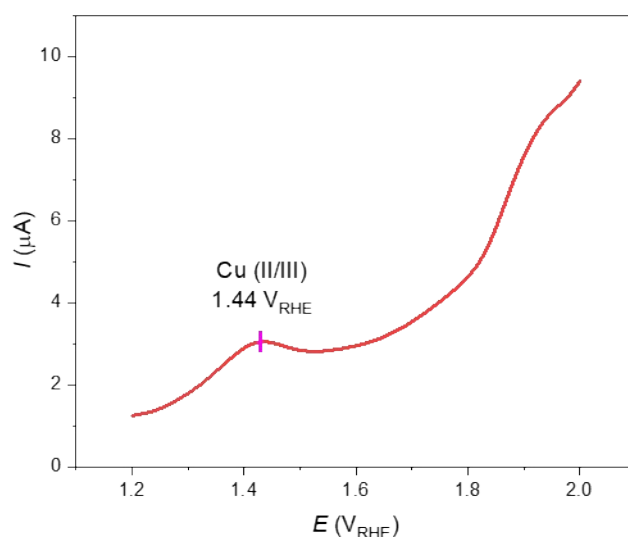


Figure S31. Differential pulse voltammogram of Cu₄-dap (1 mM) in Na₂HPO₄ buffer (0.1 M, pH 11.5, $I = 0.44$ M).

19. The scan rate dependence of observed currents with Cu₄-dap in CV

CV measurements of Cu₄-dap were carried out at 25 °C with CHI760E potentiostat (CH Instruments, Inc., TX, US) with different scan rates (2–200 mV/s). Cu₄-dap solution (1 mM) prepared in Na₂HPO₄ buffer (0.1 M, pH 11.5, I = 0.44 M) was transferred to an electrolysis cell equipped with GC electrode (S = 0.071 cm²), Ag/AgCl (reference electrode), and Pt wire (counter electrode). The solution was bubbled with N₂ over 15 min to remove dissolved O₂.

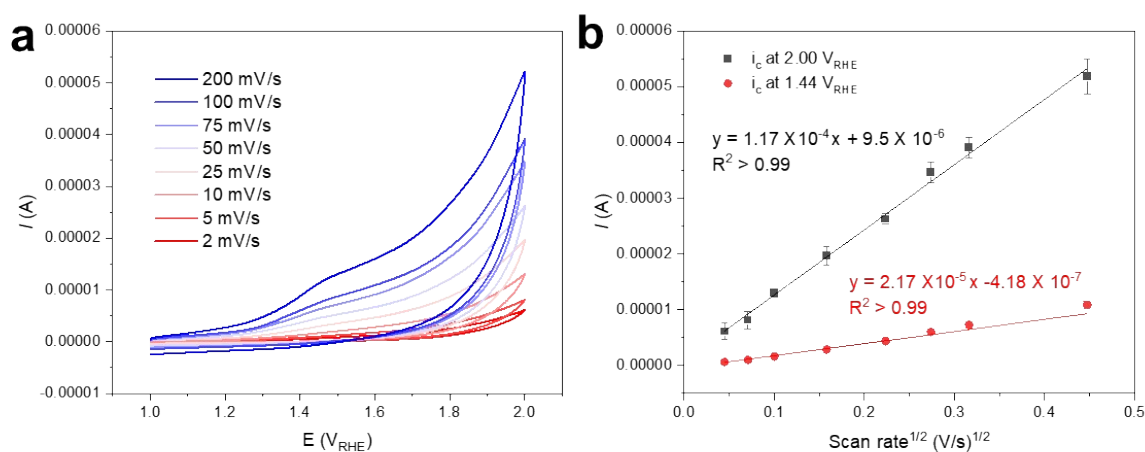


Figure S32. (a) Cyclic voltammograms of Cu₄-dap with different scan rate (2–200 mV/s). (b) Plot of current versus scan rate^{1/2} (V/s)^{1/2}. After triplicated experiments, the standard deviations were calculated and used for error bars.

20. Faradaic efficiency evaluation during water electrolysis

As shown in Figure S33, Faradaic efficiency (FE) for O₂ formation was evaluated with a potentiostat (VMP3, Bio-Logic Science Ins., FR) in a two-compartment electrochemical cell, where the anode and cathode parts were separated by an ion-conducting membrane at 25 °C. The working electrode was a glassy carbon (GC) plate with an active surface area of 1 cm², submerged in the anolyte of Na₂HPO₄ buffer (0.1 M, pH 11.5, *I* = 0.44 M) containing Cu₄-dap (1 mM). The saturated Ag/AgCl and graphite electrodes were used as reference and counter electrodes, respectively. The evolution of O₂ from water electrolysis was measured using a fiber-optic O₂ sensor (FireStingO₂, PyroScience, Aachen, GE) at a potential of 1.9 V_{RHE} for 1 h. Before the measurement, both anolyte and catholyte were vigorously purged with pure Ar gas. To prevent interference from the atmospheric O₂, the electrochemical cell kept air-tight during the measurement. The oxygen was measured by the oxygen sensor in % and converted to μmol using a calibration curve. The calibration curve was constructed by the gradual addition of the known amount of pure oxygen (μmol) into the cell containing buffer solution using a Hamilton syringe while measuring the oxygen in % by the oxygen sensor and then by plotting the amount of pure oxygen added (μmol) versus the read of oxygen sensor (%) (Figure S34). Totally accumulated charge (Q) on GC plate with correction of background obtained from bare GC was 3.571 C for 1 h. Following Eq. S9, FE of 54% with Cu₄-dap for O₂ formation was obtained (Figure S35).

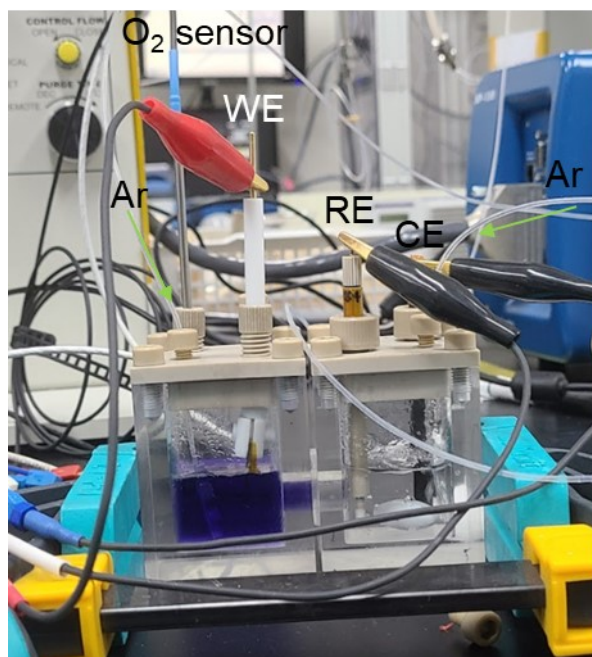


Figure S33. Photograph of air-tight electrolysis cell employed to measure FE for OER.

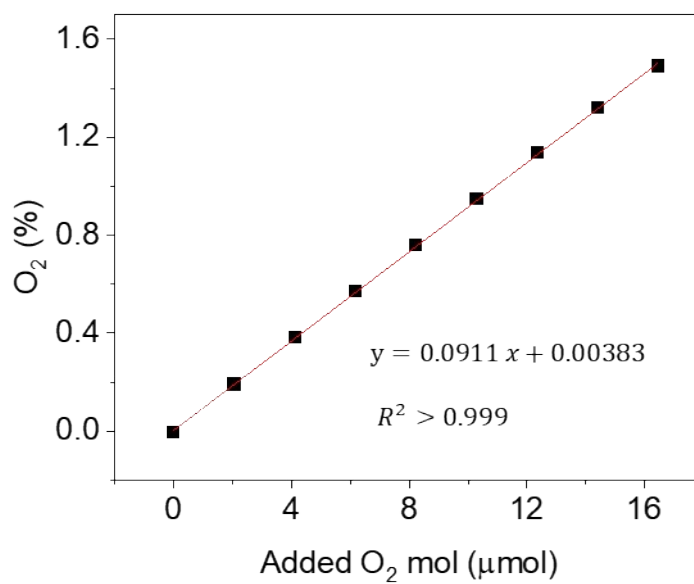


Figure S34. O₂ calibration curve to convert the read of the oxygen sensor (%) to the number of moles (μmol).

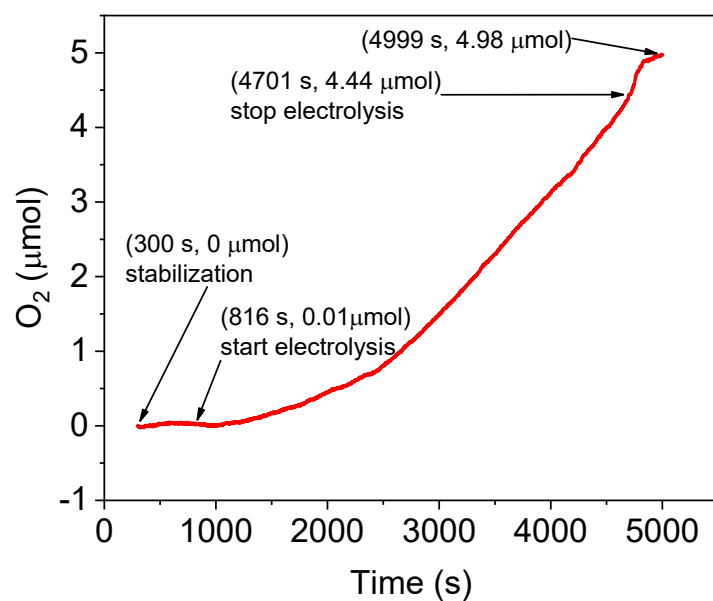


Figure S35. The amount of evolved O₂ under the applied potential of 1.9 V_{RHE} measured for the Cu₄-dap complex solution (1 mM) in Na₂HPO₄ buffer (0.1 M, pH 11.5, I = 0.44 M) at 25 °C.

$$FE (\%) = \frac{4 \times O_2(\text{mol}) \times F}{Q} \times 100 \quad (\text{Eq. S9})$$

where, F = 96485.333 C/mol

21. *In situ* UV-vis spectroscopy

In situ UV-vis spectroscopy was conducted by measuring the UV-vis spectra during electrolysis using a UV-vis spectrometer (Genesis 180, Thermo-Fischer Scientific, US) equipped with a quartz cell (path length = 1 cm) at 25 °C. Electrolysis was carried out with a potentiostat (VMP3, Bio-Logic Science Ins., FR) and a carbon paper (working electrode, MGL 190, AvCarb, US) in the quartz cell equipped with a doubly separated Ag/AgCl reference electrode (RE-16 for strong alkaline media, polyether ether ketone body (PEEK), EC-Frontier) and a carbon paper counter electrode (MGL 190, AvCarb, US). The constant potential of 1.8 V_{RHE} was applied into the Cu₄-dap complex solution (0.25 mM) in Na₂HPO₄ buffer (0.1 M, pH 11.5, I = 0.44 M) for 30 min at 25 °C.

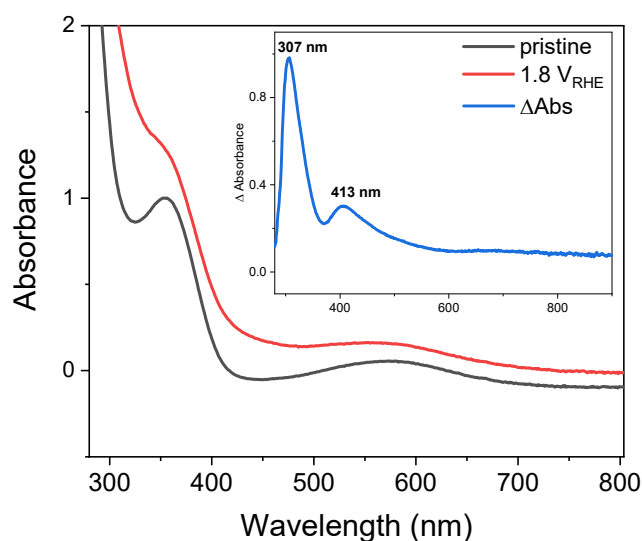


Figure S36. *In situ* UV-vis spectroscopy for Cu₄-dap during OER. The UV-vis spectra of Cu₄-dap (0.25 mM) were measured without an applied potential (black line) and with the applied potential of 1.8 V_{RHE} (red line) in Na₂HPO₄ buffer (0.1 M, pH 11.5, I = 0.44 M). The difference of absorbance was presented in blue line.

22. *In situ* Raman spectroscopy

All the *in situ* Raman experiments were performed at 25 °C with a Raman spectrometer (LabRAM HR Evolution, Horiba, JP) with a 50X long working distance visible objective. The wavelength of the excitation light source was 532 nm, with a spectral range of 200–1700 cm^{-1} . To establish the reliability of the acquired Raman spectra, the Raman shift was accurately calibrated using a silicon standard sample (520.6 cm^{-1}). All the individual Raman spectra were obtained with an acquisition time of 300 s with a grating of 600 g/mm. *In situ* Raman experiments were performed with a three-electrode configuration and custom-made electrochemical cell at 25 °C. For the *in situ* measurements, glassy carbon electrodes with a thickness of 1 mm were used as the working electrode and $\text{Cu}_4\text{-dap}$ complexes (5 mM in 0.1 M Na_2HPO_4 buffer, pH 11.5, $I = 0.44$ M) were prepared. The counter electrode was a platinum foil, and the reference electrode was Ag/AgCl (3.0 M NaCl, BASi, US). All the Raman spectra were collected at open circuit potential (OCP) and under individual applied potential where the chronoamperometry analyses were performed using a potentiostat (CHI 600E, CH Instruments, Inc., TX, US).

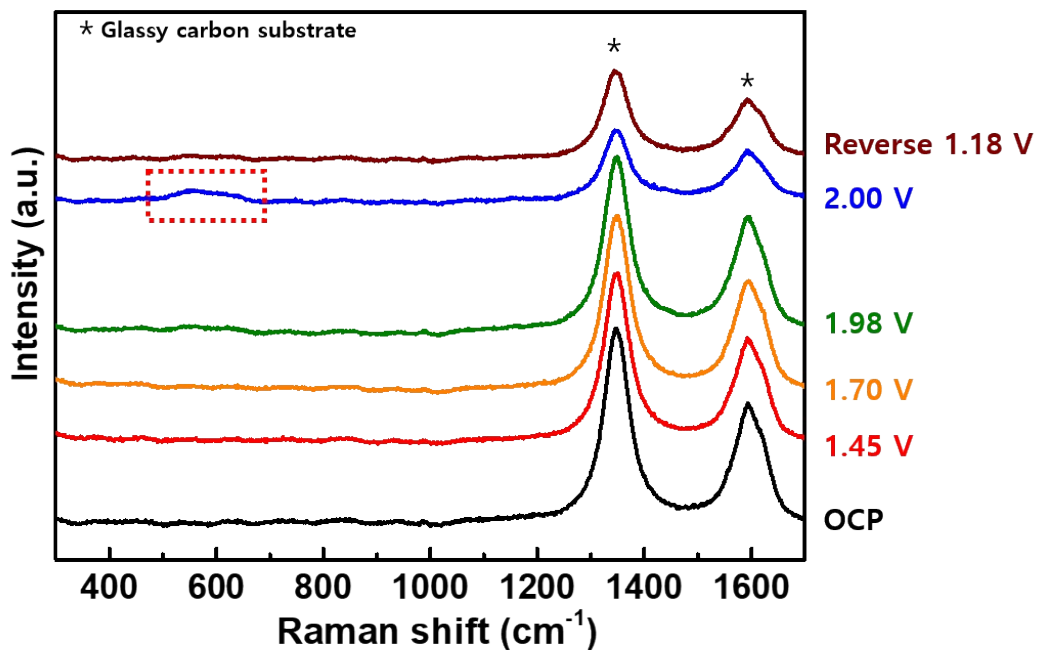


Figure S37. Potential-dependent *in situ* Raman spectra of Cu₄-dap complexes (5 mM) upon increasing the applied potential from OCP to 2.0 V and at reversely applied potential in Na₂HPO₄ buffer (0.1M, pH 11.5, *I* = 0.44 M). All the potentials are relative to RHE.

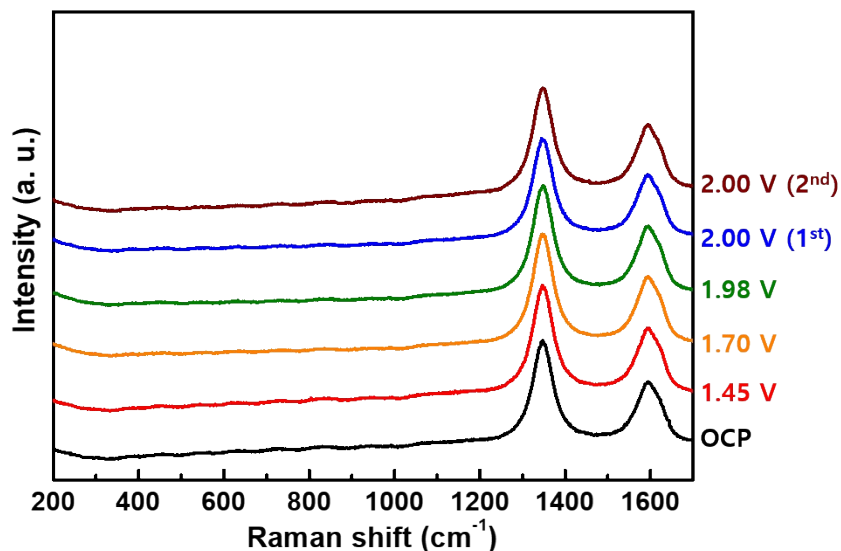


Figure S38. Potential-dependent *in situ* Raman spectra of Cu₁-dap (5 mM) complexes upon increasing the applied potential from OCP to 2.0 V in Na₂HPO₄ buffer (0.1M, pH 11.5, *I* = 0.44 M). No new peak was observed in Cu₁-dap complexes. All the potentials are relative to RHE.

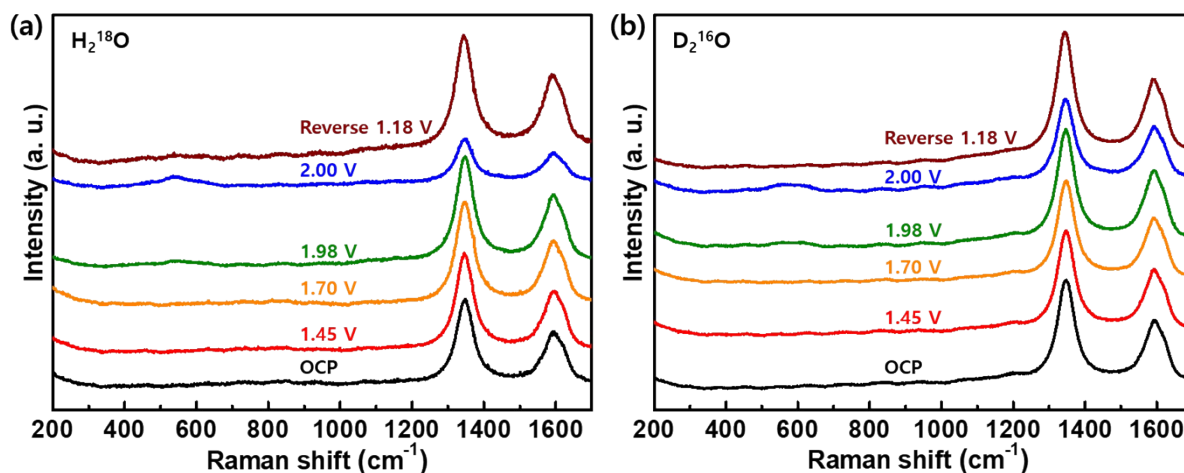


Figure S39. Potential-dependent *in situ* Raman spectra of Cu_4 -dap complexes obtained in Na_2HPO_4 buffer (0.1 M, pH 11.5, $I = 0.44$ M) containing (a) H_2^{18}O and (b) D_2^{16}O . All the potentials are relative to RHE.

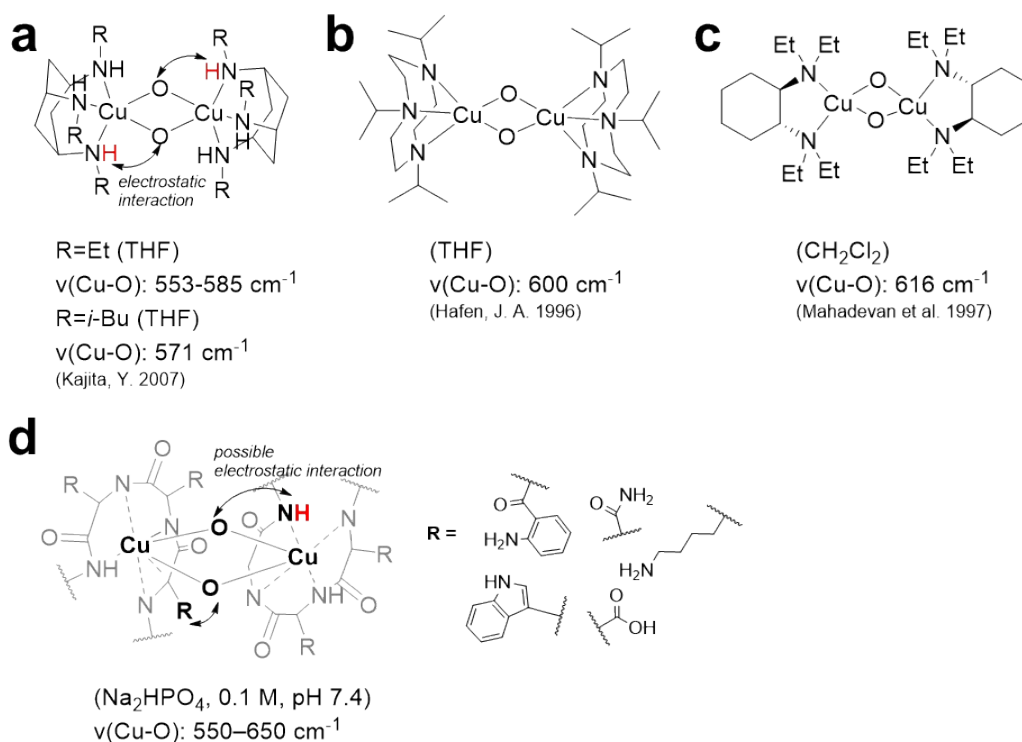


Figure S40. Previously assigned Raman shifts of $\nu(\text{Cu-O})$ in *bis- μ -oxo- Cu_2* complexes: (a)¹⁴, (b)²⁸ and (c)²⁹. (d) The expected *bis- μ -oxo- Cu_2* core on peptide backbone of daptomycin with additional interactions afforded by neighboring functional groups.

23. Kinetic isotope effect in CV measurement

CV analysis of Cu₄-dap (1 mM) were carried out at 25 °C with H₂O or D₂O in Na₂HPO₄ buffer (0.1 M) (pH 11.5 and pH* 11.9 for buffer prepared in H₂O and D₂O, respectively) to evaluate the kinetic isotope effect of current density. An electrolysis cell equipped with a 3-electrode system (working electrode: GC (S= 0.071 cm²), reference electrode: Ag/AgCl, and counter electrode: Pt wire) and CHI760E potentiostat (CH Instruments, Inc., TX, US) were used to measure cyclic voltammograms at scan rate of 0.1 V/s.

24. A plausible reaction pathway for O–O bond formation mediated by Cu₄-dap

A plausible OER mechanism, consistent with our spectroscopic and electrochemical analysis, is proposed on Figure S41. The proposed reaction pathway starts with two Cu(II)-OH sites in a resting state, revealed in the EPR analysis. In path *a*, these two sites will be oxidized to a high-valent Cu(III)-OH species without involvement of proton supported by the observed small KIE (1.1 for *i_d*) for Cu(III) formation (Figure 5d). To form *bis-μ-oxo*-Cu₂ intermediate, observed using *in situ* Raman and UV-vis spectroscopy (Figures 5c and S36), we expected path *b* and *c*, which are responsible for Cu dimerization and deprotonation, respectively. Of course, a real reaction mechanism for path *b* and *c* might be composed of highly complicated kinetics due to a flexible and less defined nature of Cu_n-dap complexes. In path *d*, the O–O bond formation may proceed without proton involvement by radical coupling (RC) in the Cu₂O₂ cores providing *trans-μ-1,2-peroxo*-Cu₂ species, which is often suggested for homogeneous Cu electrocatalyst for OER.^{8, 10, 11, 19, 30-32} This O–O bond formation mechanism is supported by the observed intermediates in the *in situ* Raman spectra (Figure 5c) and the negligible KIE (1.0 for *i_c*) in the CVs (Figure 5d). After a further two-electron oxidation step, O₂ is produced, and the Cu(II)-OH moieties can be regenerated.

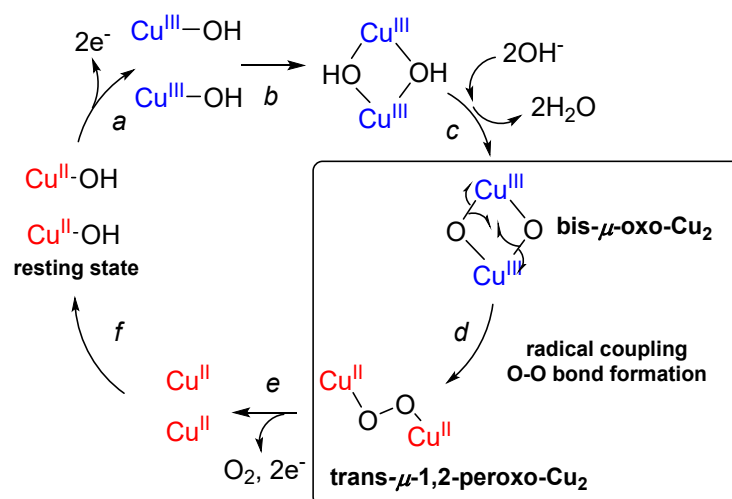


Figure S41. A plausible reaction pathway for O–O bond formation during electrochemical OER with Cu₄-dap catalyst.

25. Reference

1. L. D. Pettit, K. J. Powell, R. W. Ramette and M. Koether, SolEq: solution equilibria, principles and applications (Freeware), Academic Software, Otley, U.K., 1999.
2. T. M. Powers, The Evans Method, <https://www.jove.com/science-education/10304>, (accessed 05-25-2021, 2021).
3. S. Stoll and A. Schweiger, EasySpin, a comprehensive software package for spectral simulation and analysis in EPR, *J. Magn. Reson.*, 2006, **178**, 42-55.
4. S. Yoganathan, N. Yin, Y. He, M. F. Mesleh, Y. G. Gu and S. J. Miller, An efficient chemical synthesis of carboxylate-isostere analogs of daptomycin, *Org. Biomol. Chem.*, 2013, **11**, 4680-4685.
5. K. Takehara and Y. Ide, Electrochemistry of Cu(II)-peptide complexes containing histidine residues II. Anomalous current fluctuation in the reduction process of Cu(II)-GGH, *Inorganica Chimica Acta*, 1991, **186**, 73-78.
6. C. Hureau, H. Eury, R. Guillot, C. Bijani, S. Sayen, P. L. Solari, E. Guillon, P. Faller and P. Dorlet, X-ray and solution structures of Cu(II) GHK and Cu(II) DAHK complexes: influence on their redox properties, *Chem. Eur. J.*, 2011, **17**, 10151-10160.
7. V. A. Streltsov, R. S. K. Ekanayake, S. C. Drew, C. T. Chantler and S. P. Best, Structural insight into redox dynamics of copper bound N-truncated amyloid-β peptides from *in situ* X-ray absorption spectroscopy, *Inorg. Chem.*, 2018, **57**, 11422-

- 11435.
8. T. T. Li and Y. Q. Zheng, Electrocatalytic water oxidation using a chair-like tetranuclear copper(II) complex in a neutral aqueous solution, *Dalton Trans.*, 2016, **45**, 12685-12690.
 9. F. Yu, F. Li, J. Hu, L. Bai, Y. Zhu and L. Sun, Electrocatalytic water oxidation by a macrocyclic Cu(II) complex in neutral phosphate buffer, *Chem. Commun.*, 2016, **52**, 10377-10380.
 10. X. J. Su, M. Gao, L. Jiao, R. Z. Liao, P. E. Siegbahn, J. P. Cheng and M. T. Zhang, Electrocatalytic water oxidation by a dinuclear copper complex in a neutral aqueous solution, *Angew. Chem. Int. Ed.*, 2015, **54**, 4909-4914.
 11. G. Ruan, P. Ghosh, N. Fridman and G. Maayan, A di-copper-peptoid in a noninnocent borate buffer as a fast electrocatalyst for homogeneous water oxidation with low overpotential, *J. Am. Chem. Soc.*, 2021, **143**, 10614-10623.
 12. M. T. Zhang, Z. Chen, P. Kang and T. J. Meyer, Electrocatalytic water oxidation with a copper(II) polypeptide complex, *J. Am. Chem. Soc.*, 2013, **135**, 2048-2051.
 13. S. M. Barnett, K. I. Goldberg and J. M. Mayer, A soluble copper-bipyridine water-oxidation electrocatalyst, *Nat. Chem.*, 2012, **4**, 498-502.
 14. Y. Kajita, H. Arai, T. Saito, Y. Saito, S. Nagatomo, T. Kitagawa, Y. Funahashi, T. Ozawa and H. Masuda, Syntheses, characterization, and dioxygen reactivities of Cu(I) complexes with *cis,cis*-1,3,5-triaminocyclohexane derivatives: a Cu(III)₂O₂ intermediate exhibiting higher C-H activation, *Inorg. Chem.*, 2007, **46**, 3322-3335.
 15. D. Jiang, X. Li, L. Liu, G. B. Yagnik and F. Zhou, Reaction rates and mechanism of the ascorbic acid oxidation by molecular oxygen facilitated by Cu(II)-containing amyloid-beta complexes and aggregates, *J. Phys. Chem. B*, 2010, **114**, 4896-4903.
 16. D. Kim, N. H. Kim and S. H. Kim, 34 GHz pulsed ENDOR characterization of the copper coordination of an amyloid beta peptide relevant to Alzheimer's disease, *Angew. Chem. Int. Ed.*, 2013, **52**, 1139-1142.
 17. S. N. Semenov, L. Belding, B. J. Cafferty, M. P. S. Mousavi, A. M. Finogenova, R. S. Cruz, E. V. Skorb and G. M. Whitesides, Autocatalytic cycles in a copper-catalyzed azide-alkyne cycloaddition reaction, *J. Am. Chem. Soc.*, 2018, **140**, 10221-10232.
 18. R. Kotuniak, M. J. F. Strampraad, K. Bossak-Ahmad, U. E. Wawrzyniak, I. Ufnalska, P. L. Hagedoorn and W. Bal, Key intermediate species reveal the Copper(II)-exchange pathway in biorelevant ATCUN/NTS complexes, *Angew. Chem. Int. Ed.*,

- 2020, **59**, 11234-11239.
19. J. Shen, M. Wang, P. Zhang, J. Jiang and L. Sun, Electrocatalytic water oxidation by copper(II) complexes containing a tetra- or pentadentate amine-pyridine ligand, *Chem. Commun.*, 2017, **53**, 4374-4377.
 20. T. Ghosh, P. Ghosh and G. Maayan, A copper-peptoid as a highly stable, efficient, and reusable homogeneous water oxidation electrocatalyst, *ACS Catal.*, 2018, **8**, 10631-10640.
 21. J. T. Pedersen, S. W. Chen, C. B. Borg, S. Ness, J. M. Bahl, N. H. Heegaard, C. M. Dobson, L. Hemmingsen, N. Cremades and K. Teilum, Amyloid- β and α -synuclein decrease the level of metal-catalyzed reactive oxygen species by radical scavenging and redox silencing, *J. Am. Chem. Soc.*, 2016, **138**, 3966-3969.
 22. S. Thanneeru, N. Milazzo, A. Lopes, Z. Wei, A. M. Angeles-Boza and J. He, Synthetic polymers to promote cooperative Cu activity for O₂ activation: Poly vs Mono, *J. Am. Chem. Soc.*, 2019, **141**, 4252-4256.
 23. O. V. Makhlynets, P. M. Gosavi and I. V. Korendovych, Short self-assembling peptides are able to bind to copper and activate oxygen, *Angew. Chem. Int. Ed.*, 2016, **55**, 9017-9020.
 24. B. Yang, Y. Chen and J. Shi, Reactive oxygen species (ROS)-based nanomedicine, *Chem. Rev.*, 2019, **119**, 4881-4985.
 25. K. P. Neupane, A. R. Aldous and J. A. Kritzer, Macrocyclization of the ATCUN motif controls metal binding and catalysis, *Inorg. Chem.*, 2013, **52**, 2729-2735.
 26. K. J. J. Mayrhofer, A. S. Crampton, G. K. H. Wiberg and M. Arenz, Analysis of the impact of individual glass constituents on electrocatalysis on Pt electrodes in alkaline solution, *J. Electrochem. Soc.*, 2008, **155**, 78-81.
 27. K. J. J. Mayrhofer, G. K. H. Wiberg and M. Arenz, Impact of glass corrosion on the electrocatalysis on Pt electrodes in alkaline electrolyte, *J. Electrochem. Soc.*, 2008, **155**, 1-5.
 28. J. A. Halfen, S. Mahapatra, E. C. Wilkinson, S. Kaderli, V. G. Young, L. Que, A. D. Zuberbuhler and W. B. Tolman, Reversible cleavage and formation of the dioxygen O–O band within a dicopper complex, *Science*, 1996, **271**, 1397-1400.
 29. V. Mahadevan, Z. Hou, A. P. Cole, D. E. Root, T. K. Lal, E. I. Solomon and T. D. P. Stack, Irreversible reduction of dioxygen by simple peralkylated diamine–copper(I) complexes: characterization and thermal stability of a [Cu₂(μ -O)₂]²⁺Core, *J. Am.*

Chem. Soc., 1997, **119**, 11996-11997.

30. S. J. Koepke, K. M. Light, P. E. VanNatta, K. M. Wiley and M. T. Kieber-Emmons, Electrocatalytic water oxidation by a homogeneous copper catalyst disfavors single-site mechanisms, *J. Am. Chem. Soc.*, 2017, **139**, 8586-8600.
31. X. P. Zhang, A. Chandra, Y. M. Lee, R. Cao, K. Ray and W. Nam, Transition metal-mediated O–O bond formation and activation in chemistry and biology, *Chem. Soc. Rev.*, 2021, **50**, 4804-4811.
32. M. Okamura, M. Kondo, R. Kuga, Y. Kurashige, T. Yanai, S. Hayami, V. K. Praneeth, M. Yoshida, K. Yoneda, S. Kawata and S. Masaoka, A pentanuclear iron catalyst designed for water oxidation, *Nature*, 2016, **530**, 465-468.